

AERODYNAMIC MODEL OF THE WIND HARVEST INTERNATIONAL MODEL 1500 WIND TURBINE

Prepared for

**Wind Harvest International
11431 Highway One, Suite 12
P.O. Box 358
Point Reyes Station, CA 94956-0358
USA**

Prepared by

**Dr. Ion Paraschivoiu
IOPARA Inc.
1595, Norway road
Mont-Royal town, QC, H4P 1Y3**

With comments by Robert N Thomas (in green)
and Norbert V. Dy, Dr. Farooq Saeed (in blue)

May 18, 2009

TABLE OF CONTENTS

1. Introduction	3
2. CARDAAV Aerodynamic Model Validation	4
3. Isolated Rotor Wind Turbine Aerodynamic Load Prediction using CARDAAV	6
4. Multiple Rotor Wind Turbine Aerodynamic Load Prediction using CARDAAV	15
5. Isolated Rotor Wind Turbine CFD Aerodynamic Model Calibration and Validation	16
6. Three-Rotor Wind Turbine CFD Aerodynamic Model Load Prediction.....	18
7. Parametric Study Based on 3D CFD Simulations	24
8. Conclusions	29
9. Future Work.....	29
10. Appendix 1.....	30

1. Introduction

This report is a compilation of the aerodynamic analyses of the Wind Harvest International (WHI) wind turbines, Model WHI 530 and WHI 1500, in isolated and multiple configuration settings. The aerodynamic analyses were carried out by IOPARA Inc. as a contract project for WHI from October 2008 to May 2009. The aerodynamic analyses focused on the specific tasks as requested in the project proposal. An outline of these tasks is as follows:

1. Validate aero model using WHI 530G test data from the Palm Site measurements of Cpe/blade to wind speed data, transformed into Cp (shaft power) at various wind speeds using best estimate drive train and generator efficiencies.*
2. Carryout aero model analysis runs over a 10 minute averaged wind speed range from 10 mph (4.47 m/s) and 65 mph (29 m/s) with maximum peak gust of 80 mph (35.7 m/s), to assess aerodynamic loads on the WHI Model 530G for the desired range of conditions.*
3. Repeat task 2 for the WHI Model 1500. **Deliverable:** Time and azimuthal position dependent blade and rotor load data in a yet to be specified structural analyses computer program.
4. Carryout aero model analysis runs at 125 mph wind speed to assess aerodynamic loads on the WHI 1500 model with the rotor in the parked position.*
5. Conduct a computational fluid dynamic (CFD) study to determine the effect of wake vortices on downstream turbines in a multiple turbine configuration. The study will be based on the specific arrangement of the multiple turbines as provided by WHI. This study will encompass the following tasks
 - a. Review of literature on similar studies and the various approaches used for analysis of multiple VAWT configurations
 - b. Study of the patented work and related studies/patents to gain better understanding of the underlying concepts.
 - c. Take into consideration the presence of wakes as well as associated unsteady effects of vortex shedding and viscous damping in the flow. For example, if the axis of multiple VAWTs is aligned with the wind direction, the downstream VAWTs will be operating in the wake of upstream VAWTs. Thus, the effect of wake on vortex augmentation can truly be realized in such a model. Studies of such nature have been performed for HAWTs in a wind farm setting and much can be gleaned from these studies. However, literature survey reveals that only a few studies related to VAWTs have been performed to date but as isolated VAWTs.
 - d. Develop a CFD model for the multiple turbine configuration.*
 - e. Analyze different test conditions with the CFD model and compare the numerical simulation with the vortex effect test data of the Model 530G (Cp) to validate the CFD aero model.*
 - f. Repeat Task 3 using the CFD aero model of the flow field with the vortex effect.*
 - g. Develop an empirical correction for wake effects in the aero model for multiple VAWTs operating in the wake of upstream VAWTs.
6. Carry out parametric study to determine optimal conditions for vortex augmentation.
 - a. Study effect of VAWT spacing and multiple VAWT axis orientation with respect to wind direction.
 - b. Determine the effect of the following on vortex augmentation

* First priority tasks

- i. VAWT spacing
 - ii. Multiple VAWT axis orientation with respect to wind direction with and without the wake effect model.
 - iii. Effect of VAWT solidity (blade length, chord, and rotor diameter, etc.)
 - iv. Effect of tip-speed ratio
 - v. Effect of wind speed
 - vi. Effect of blade shape (thickness)
 - vii. A combination of the above effects as desired by WHI
7. Summarize all work and results in a comprehensive report.

2. CARDAAV Aerodynamic Model Validation

The first task was performed to validate the aerodynamic model of the WHI 530G model wind turbine using the IOPARA Inc.'s in-house wind turbine analysis and design code, CARDAAV. The calibration of the CARDAAV code for the WHI 530G model was realized through adjustments of the input parameters in an effort to reproduce the experimental power coefficient values provided by WHI. For the 6-bladed WHI 1500 model, the calibration was realized by using the data presented in the report "*Evaluation of the Windstar 1500 vertical axis wind turbine system*", prepared by David J. Malcolm on September 18, 2007. If the CARDAAV code was calibrated using the 530G field test data to calculate the Model 530 Cp data and blade loading, why did it need to be recalibrated using the 1500 data in David's report to calculate the Model 1500 Cp and blade load data for the Model 1500. (David's data was taken from my Performance Manual where I estimated Cp improvements of the 1500 over the 530 due to increased blade aspect ratio, higher Reynolds number and fewer blade connections). Consequently, calibration of CARDAAV is based on performance estimates from field data of the aerodynamically similar model 530. Why was it not possible to use the Model 530 data calibration of CARDAAV to calculate the Model 1500 performance without further calibration. Does this infer that aerodynamic similitude is not satisfied by only having equal solidity and having blades of the same profile shape? RNT {The coefficients used for the calibration of the Model 530 are only slightly higher than the one used for the calibration of the Model 1500. Concerning the aerodynamic similitude, parametric analysis realized with CARDAAV for different number of blades while maintaining the rotor solidity at a fixed value (for a H-Darrieus VAWT) shows that the aerodynamic similarity could be applied from optimal to higher TSR values, but not necessarily for TSR lower than optimal. The optimal TSR being the one at which the maximum C_p value is reached}

Figure 2 shows the 6 bladed Model 1500 CARDAAV results only. To be consistent with Fig. 1 the calibration curve taken from David's report should appear on Fig. 2. Also, the curve is not as smooth as the one computed for the Model 530 inferring that convergence was more difficult to achieve in the Model 1500 calculations. Is this the case, if so why? RNT {Indeed, convergence was more difficult to achieve for the Model 1500. This problem comes from the WAKE algorithm, which still need some refinement.}

During the validation of the CARDAAV code, two major difficulties (related to the high solidity of the rotors) were encountered which resulted in a limited range of convergence and an over prediction of the aerodynamic performance. Increased convergence was obtained by modifying the convergence criteria, extending the TSR range of results from 1.45 to 2.82. Also, a new algorithm, WAKE, was implemented to include the influence of the upstream blade wake on the downstream half of the rotor.

This physical consideration enables a more realistic numerical approach and allowed CARDAAV to closely match the experimental data.

The effects of strut parasitic drag and center shaft wake were indirectly included since the calibration of CARDAAV was based on the experimental curves. The power coefficient validation result for the WHI 530G model is presented in Fig. 1 and reflects excellent agreement between CARDAAV prediction and the experimental test data for $\text{TSR} < 2.9$. Fig. 2 shows the power coefficient curve for the 6-bladed WHI 1500 model as predicted by CARDAAV for $\text{TSR} < 2.9$.

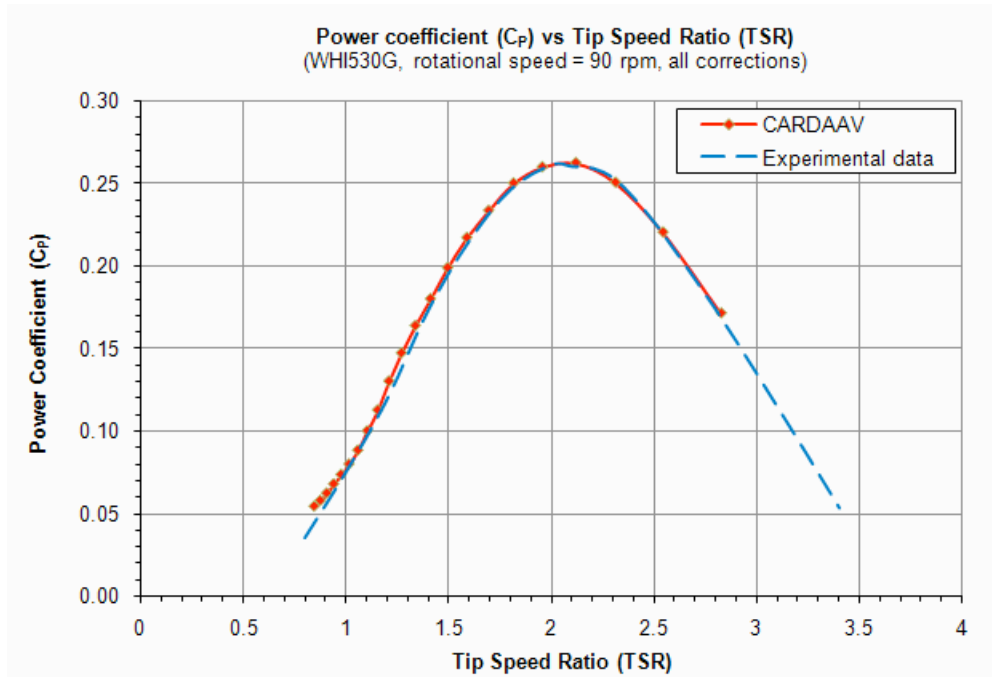


Figure 1: Comparison between CARDAAV results and experimental data for the WHI 530G

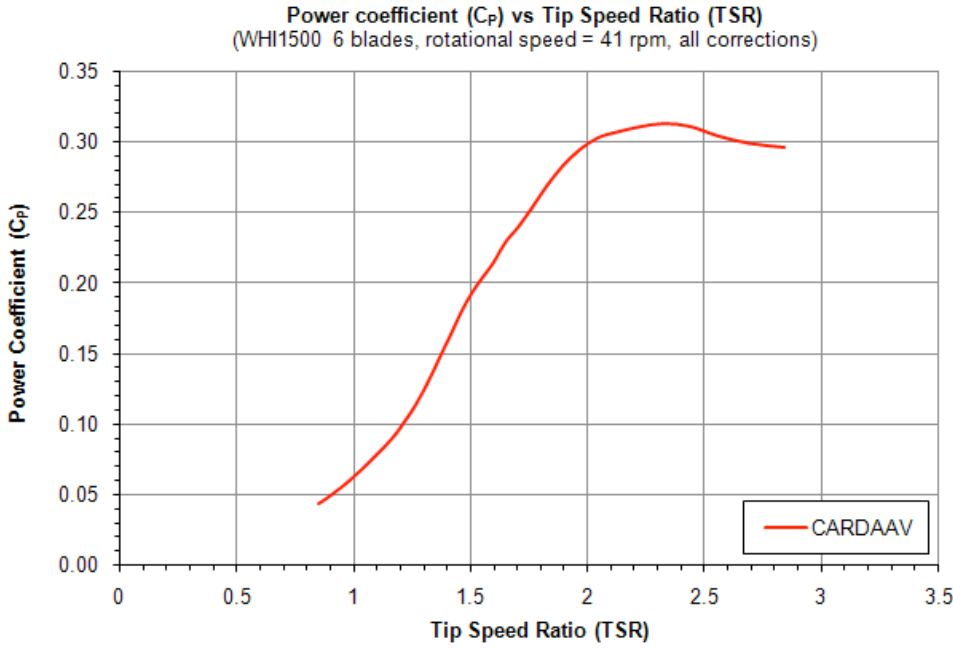


Figure 2: CARDAAV results for the 6-bladed WHI 1500 model

3. Isolated Rotor Wind Turbine Aerodynamic Load Prediction using CARDAAV

The normal and tangential forces for different blade azimuthal angular position were computed with the aid of the CADAAB code for the WHI 530G and the 6-bladed WHI 1500 models. For the WHI 530G model, the force calculations were realized at TSR values of 1.02 and 2.03 or in terms of wind speed 25 m/s and 12.5 m/s. For the WHI 1500 model, force calculations were realized at TSR values of 1.00 and 2.04 or in terms of wind speed 25.5 m/s and 12.5 m/s.

Also, please note that in CARDAAV, the following convention is used (also depicted in Fig. 3) for the azimuthal angular position:

- Looking down from directly above the rotor, the turbine is rotating counterclockwise.
- At -90° the blade is parallel to the free stream with its leading edge going upwind.
- At $+90^\circ$ the blade is parallel to the free stream with its leading edge going downwind.
- At 0° and $+180^\circ$ the blade chord is perpendicular to the free stream.
- Position -90° and $+270^\circ$ are the same.

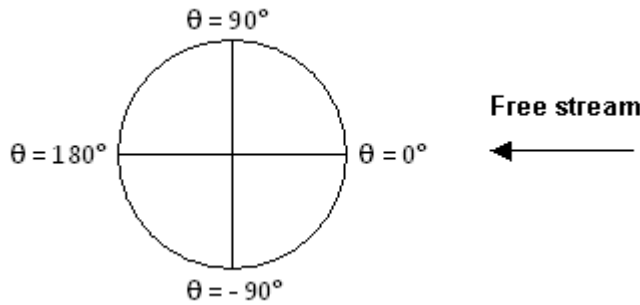


Figure 3: Azimuthal angular position in CARDAAV

The results shown in Fig. 4 to 7 represent the normal and tangential forces (N) acting on a single blade for different blade azimuthal position (deg.). What aerodynamic coefficient data was used? What airfoil? It would be helpful to have C_n and C_a (normal and axial) data as a function of angle of attack to determine angle of attack and lift and drag as a function of azimuthal angle. RNT {NACA0018 was used as airfoil for the 530 and 1500 model and the aerodynamic coefficient data come from the Sandia laboratories. The C_L and C_D as a function of the angle of attack are attached in the file NACA0018_CLD.xls}.

The results shown in Fig. 8 to 15 represent the normal and tangential force distribution (N) along the length (m) of a single blade. Those forces were calculated at critical azimuthal position i.e. the angle at which the absolute value of the normal force is maximum for the upwind and downwind half of the rotor. The vertical axis represents the force position on the blade i.e. position 0 on the vertical axis is the equatorial height of the rotor. Also, a shear wind coefficient of 0.16 was used in all calculations. Would scaling up the blade forces of the 6 bladed Model 1500 data by 6/4 approximate blade forces acting on a Model 1500 having 4 blades of 6/4 times the cord and therefore of equal solidity of the 6 bladed model? {Depending on the TSR, scaling up the normal and tangential force would be a good approximation.}

How is the wind shear coefficient defined? Is this the turbulent boundary layer exponent, $1/n$ ie a $1/n$ th profile? RNT {The wind shear coefficient is similar but different from the turbulent boundary layer exponent and links wind speed and height through the following equation:

$$\frac{V}{V_{ref}} = \left(\frac{H}{H_{ref}} \right)^{\alpha}$$

Where α is the wind shear coefficient, V is the wind speed at height H and V_{ref} is the wind speed at the reference height H_{ref} .} Also please note that some Wind Atlas use a different relationship to describe the wind shear, based on the roughness length of the terrain.

The results shown in Fig. 16 to 19 represent the value of the rotor torque (all blades included) for different azimuthal angular position (deg.) of the leading blade. The torque values are expressed in N·m.

Can we assume that a 4 bladed Model 1500 would have 6/4 times the torque amplitudes of the 6 bladed model with 6/4 times the period.? RNT {Yes for the period, but unlikely for the torque amplitude.}

Are the curves in Figs. 8 thru 15 tilted and asymmetrical about the mid blade plane because of the wind shear effect or a three dimensional effect? RNT {The tilting and asymmetry come from the wind shear effect, $\alpha = 0.16$ }

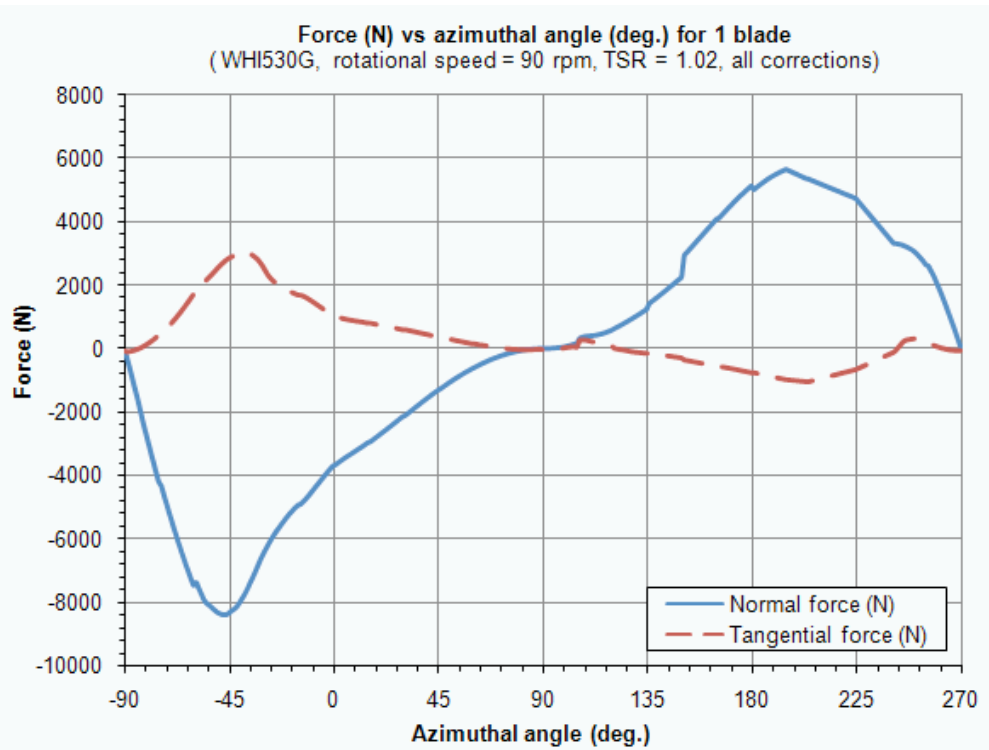


Figure 4: Normal and tangential forces (N) vs. azimuthal angle (deg.) for a single blade of the WHI 530G model at TSR = 1.02

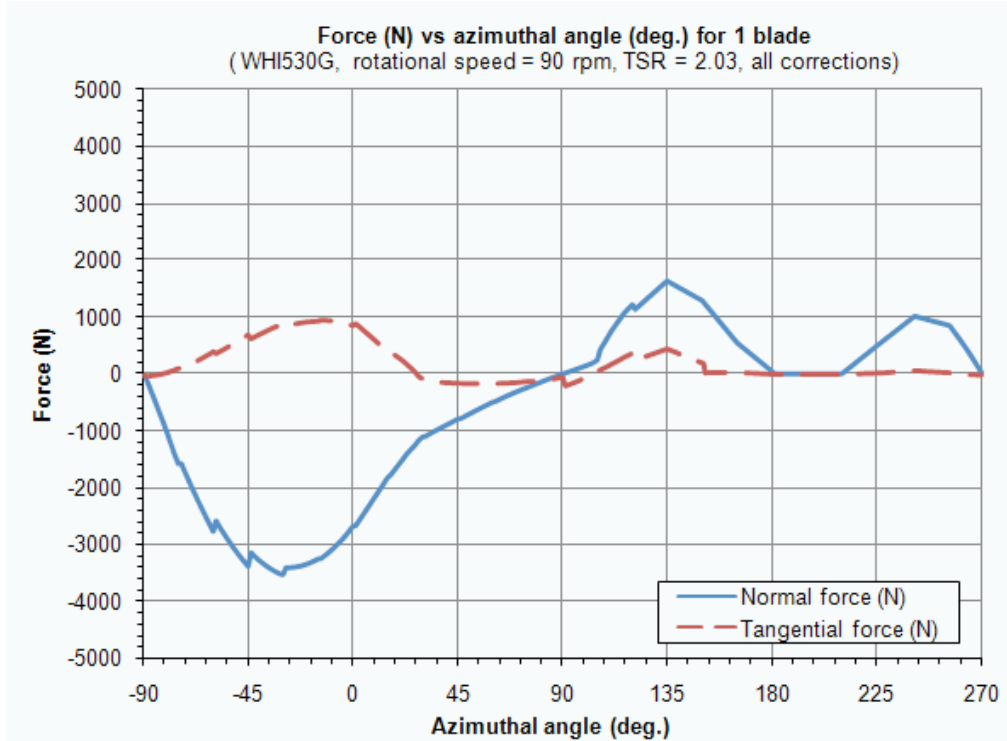


Figure 5: Normal and tangential forces (N) vs. azimuthal angle (deg.) for a single blade of the WHI 530G model at TSR = 2.03

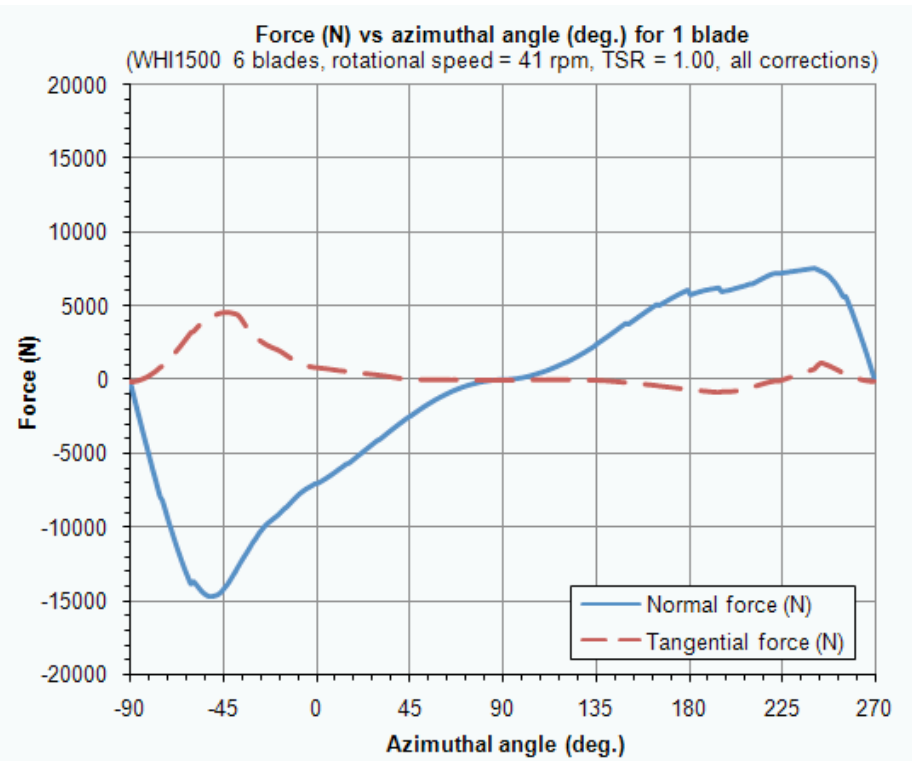


Figure 6: Normal and tangential forces (N) vs azimuthal angle (deg.) for a single blade of the 6-bladed WHI 1500 model at TSR = 1.00

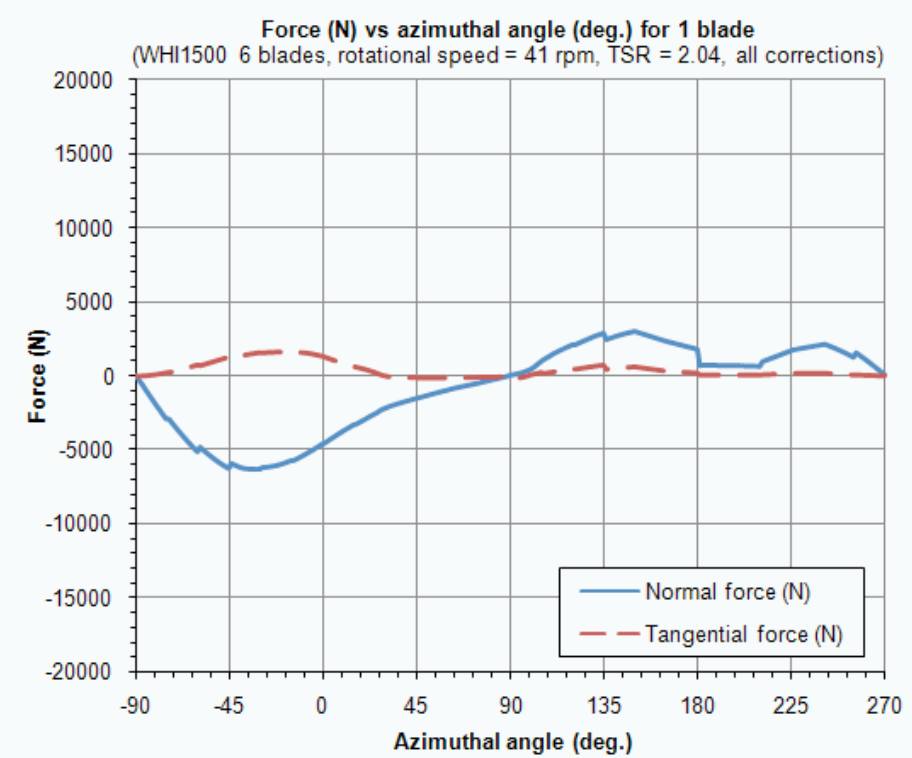


Figure 7: Normal and tangential forces (N) vs azimuthal angle (deg.) for a single blade of the 6-bladed WHI 1500 model at TSR = 2.04

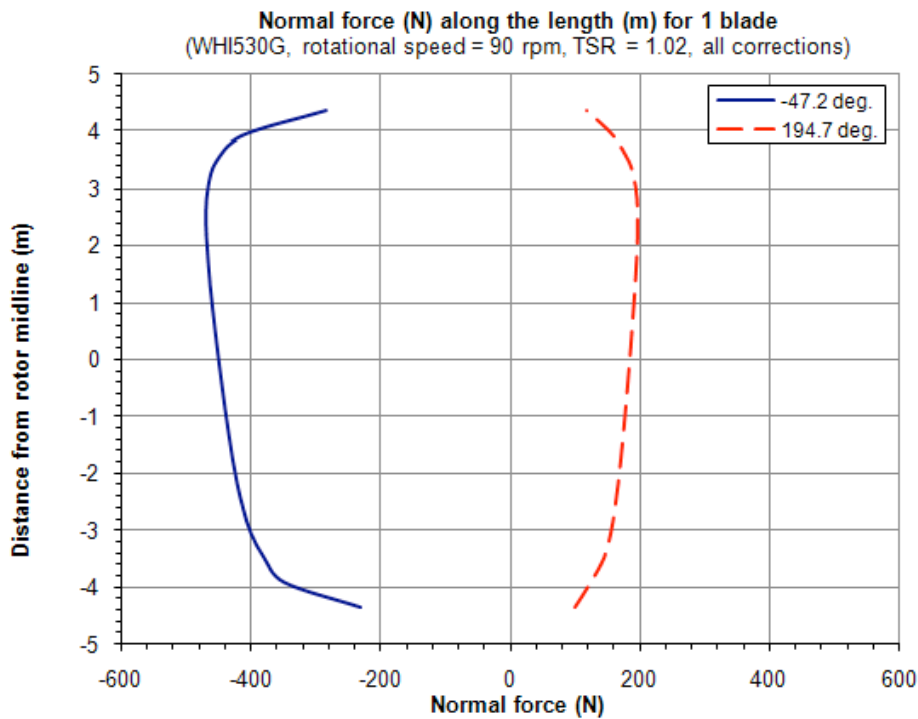


Figure 8: Normal forces (N) along the length (m) of a single blade of the WHI 530G model at TSR = 1.02

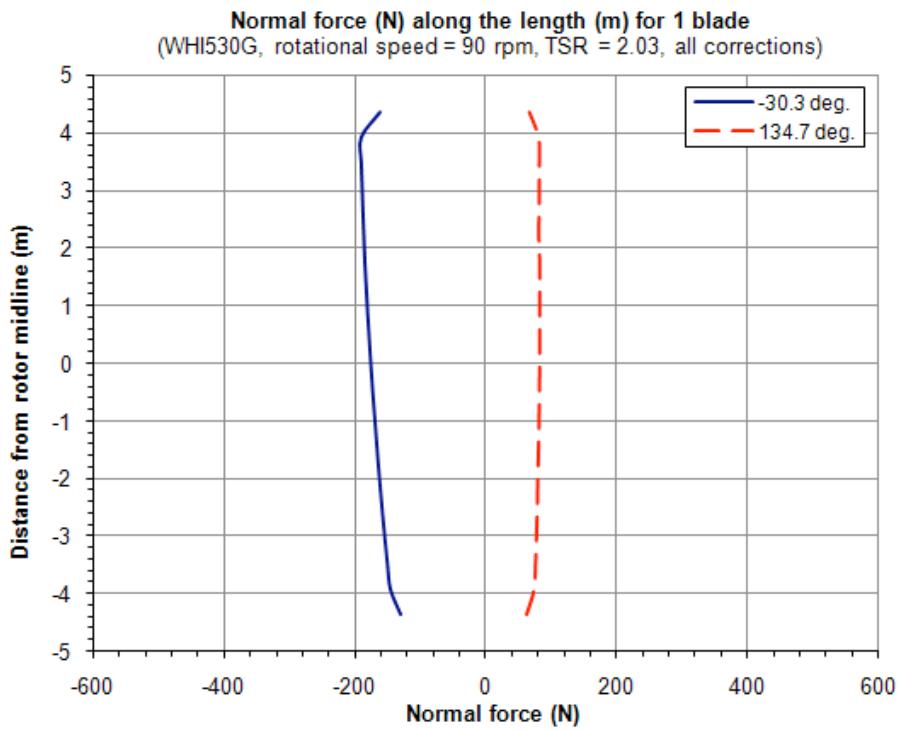


Figure 9: Normal forces (N) along the length (m) of a single blade of the WHI 530G model at TSR = 2.03

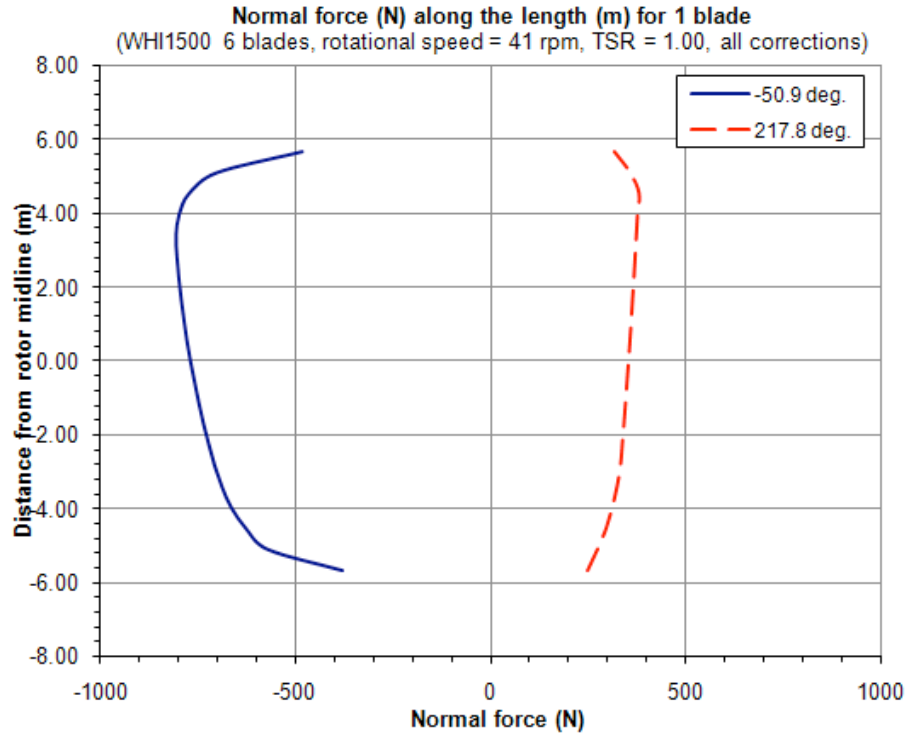


Figure 10: Normal forces (N) along the length (m) of a single blade of the 6-bladed WHI 1500 model at TSR = 1.00

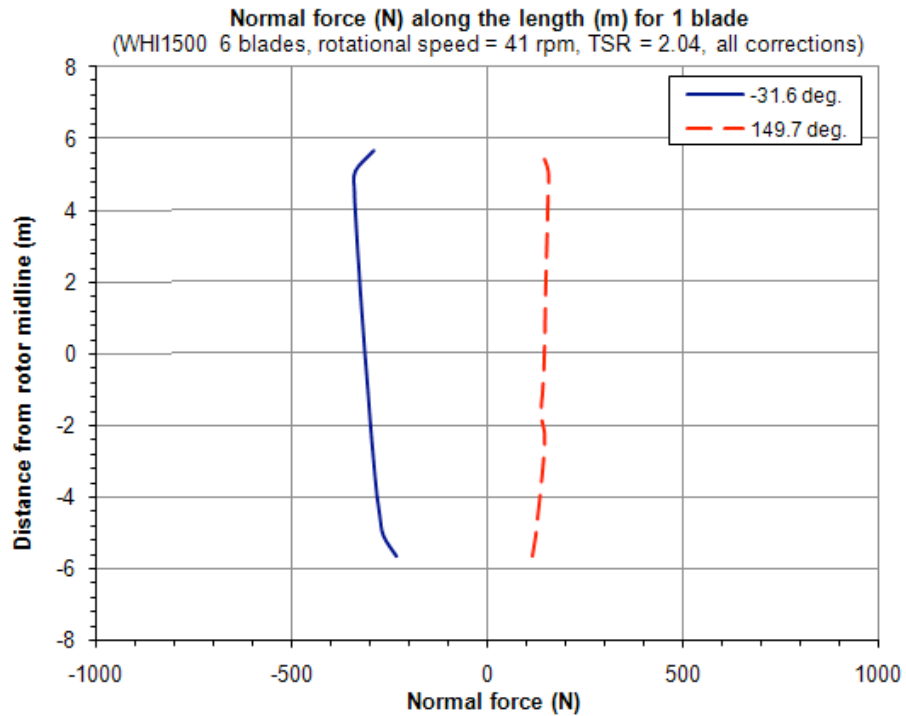


Figure 11: Normal forces (N) along the length (m) of a single blade of the 6-bladed WHI 1500 model at TSR = 2.04

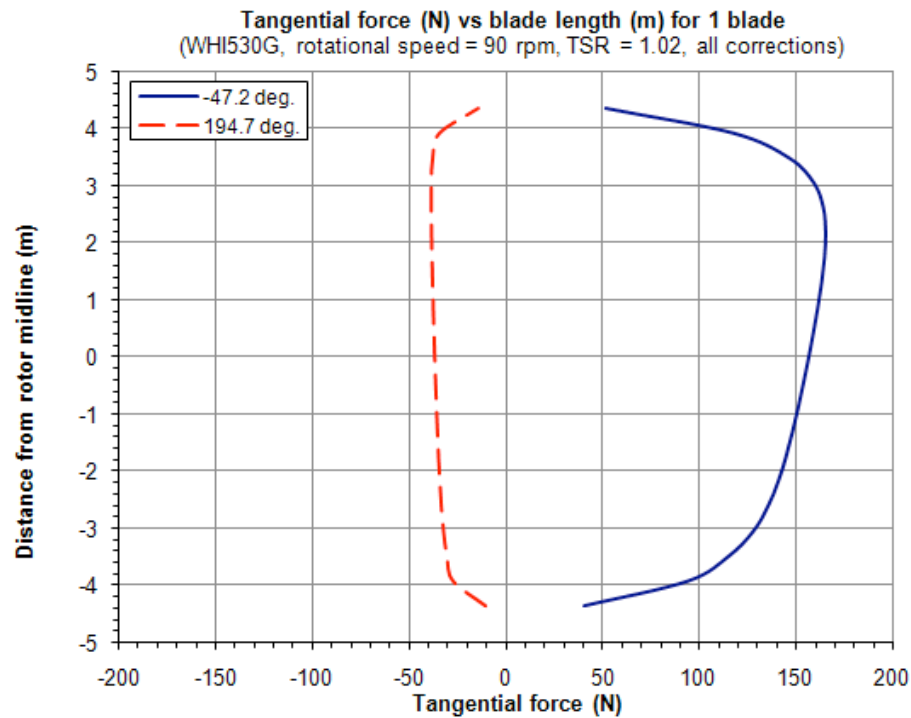


Figure 12: Tangential forces (N) along the length of a single blade of the WHI 530G model at TSR = 1.02

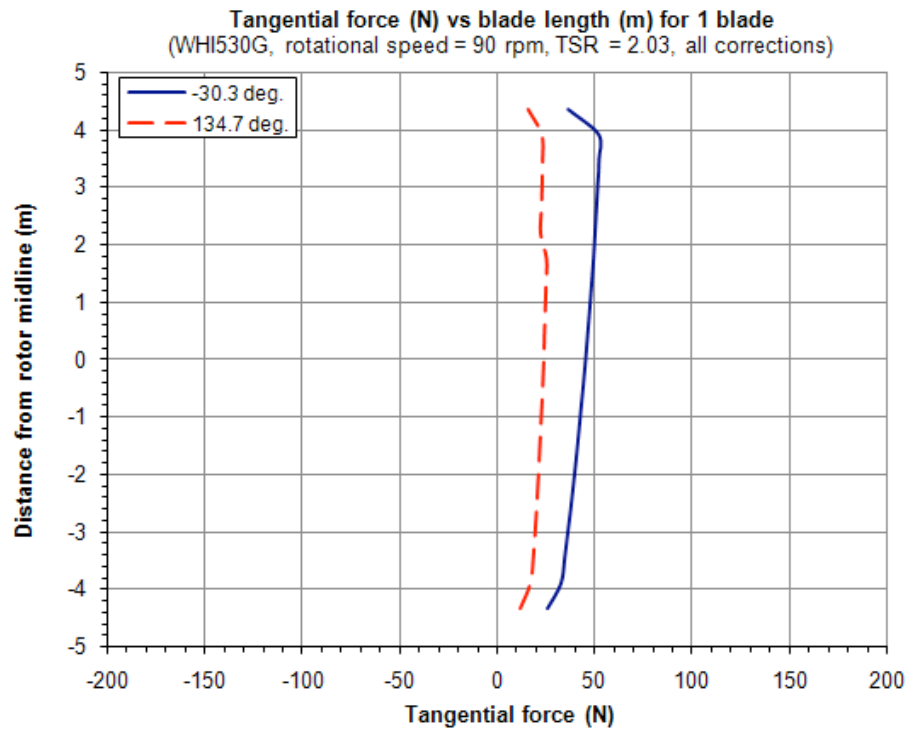


Figure 13: Tangential forces (N) along the length of a single blade of the WHI 530G model at TSR = 2.03

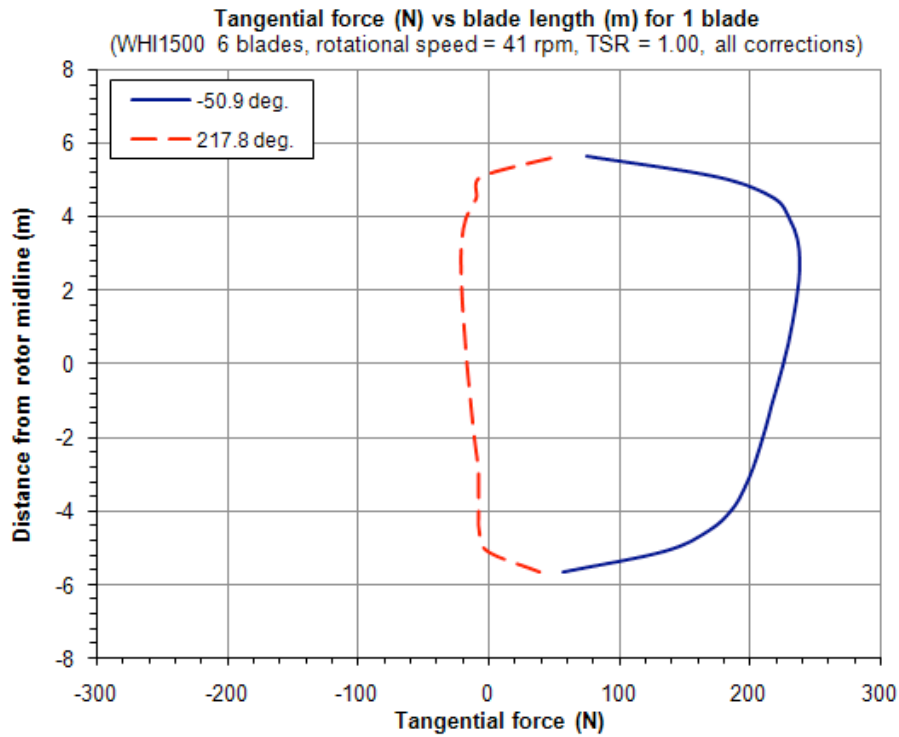


Figure 14: Tangential forces (N) along the length of a single blade of the 6-bladed WHI 1500 model at TSR = 1.00

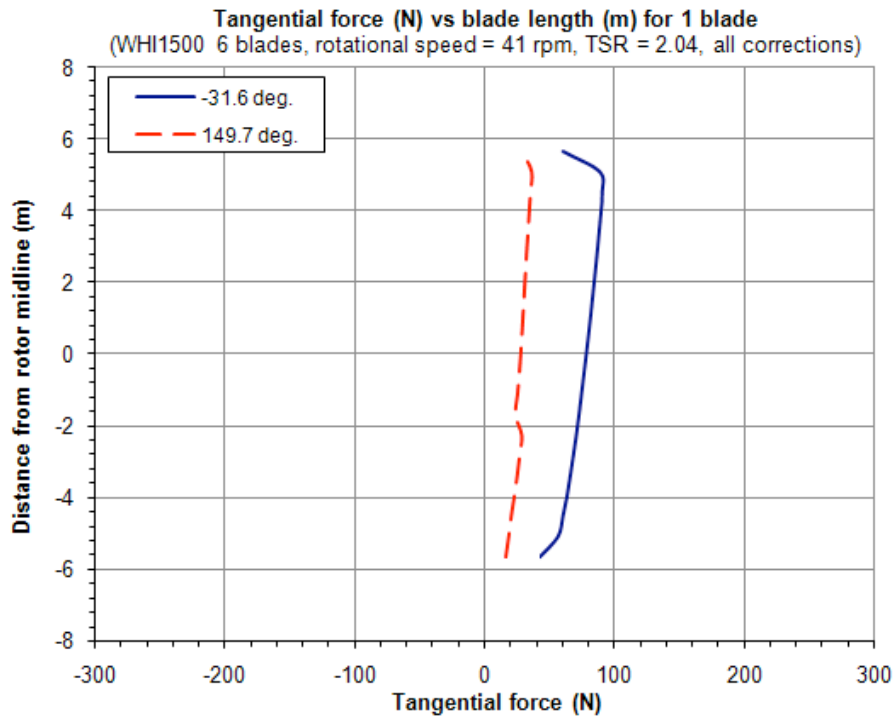


Figure 15: Tangential forces (N) along the length of a single blade of the 6-bladed WHI 1500 model at TSR = 2.04

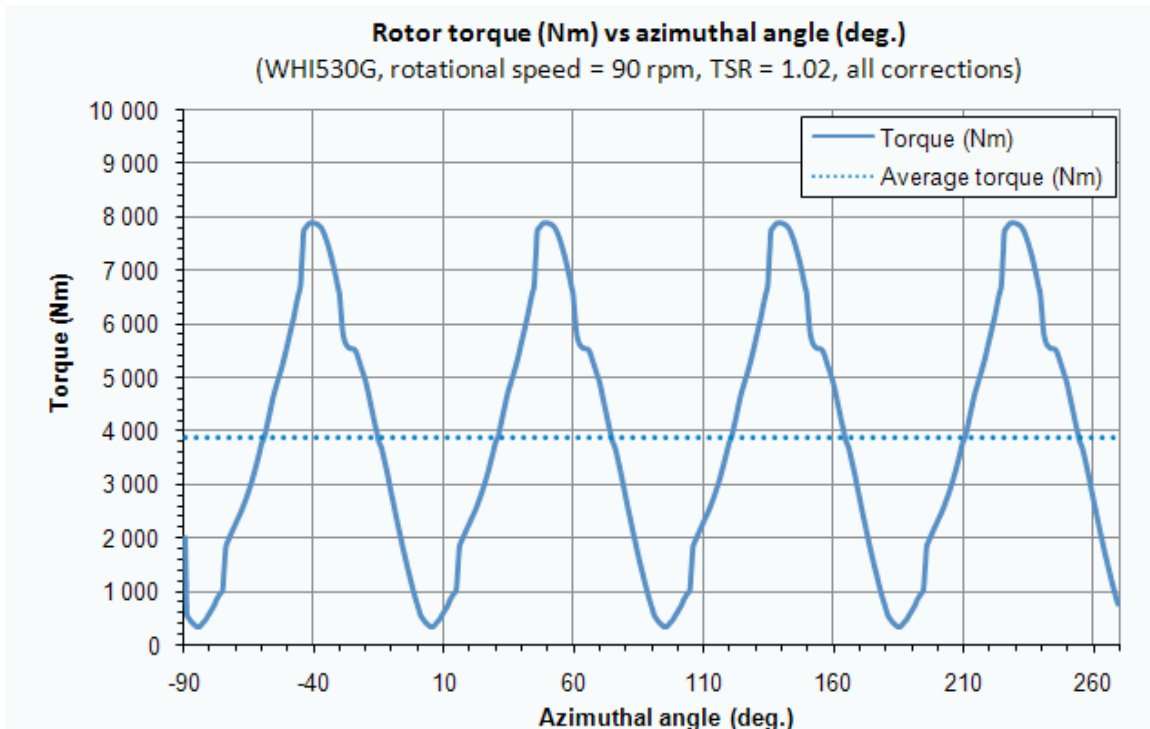


Figure 16: Rotor torque (N) vs. azimuthal angle (deg.) for the WHI 530G model at TSR = 1.02

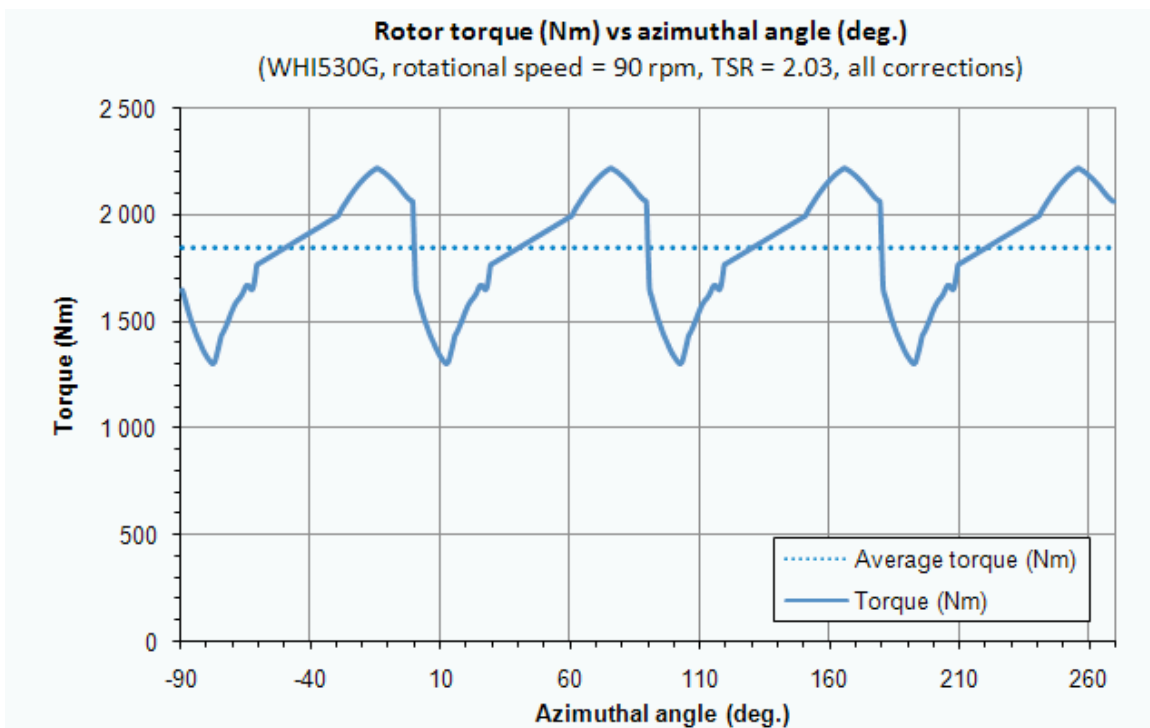


Figure 17: Rotor torque (N) vs. azimuthal angle (deg.) for the WHI 530G model at TSR = 2.03

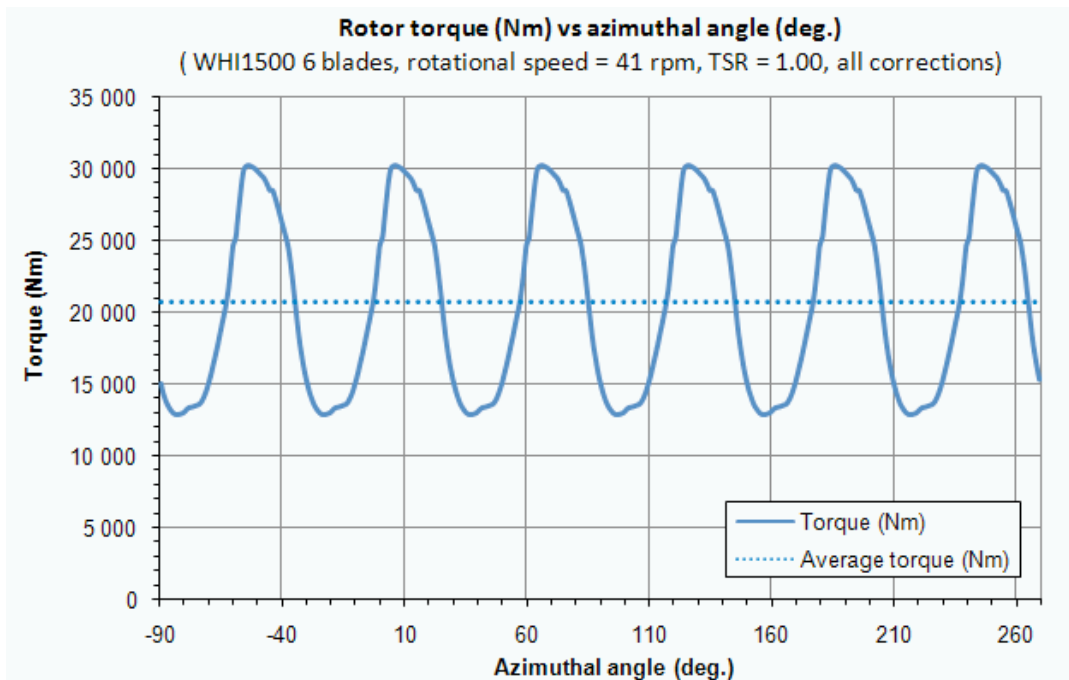


Figure 18: Rotor torque (N) vs. azimuthal angle (deg.) for the WHI 1500 model at TSR = 1.00

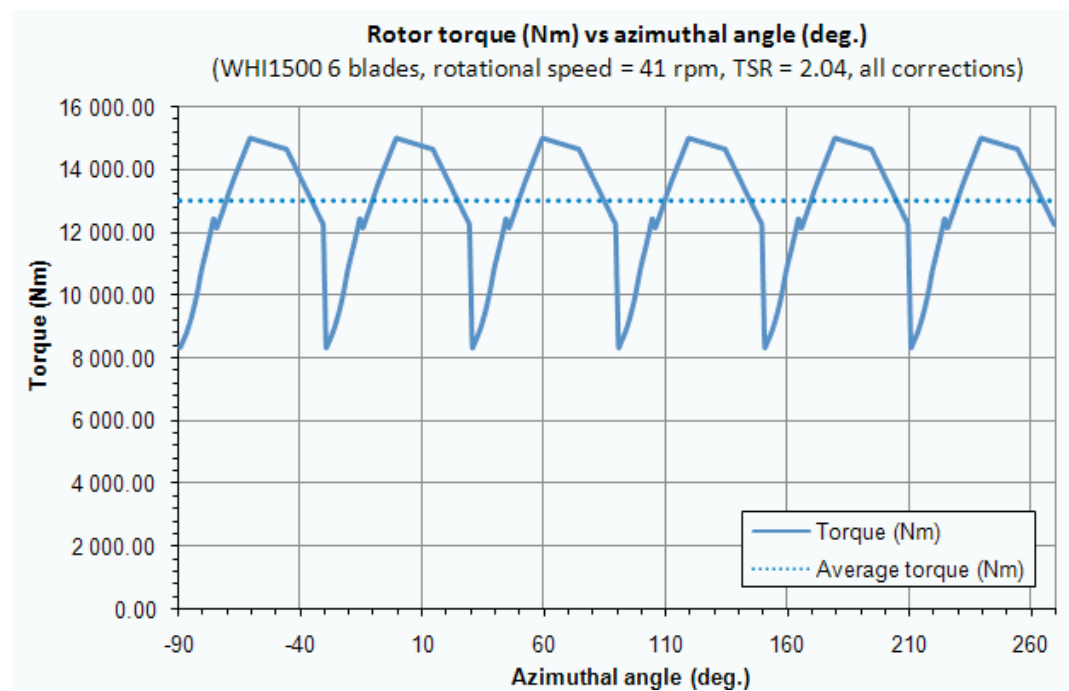


Figure 19: Rotor torque (N) vs. azimuthal angle (deg.) for the WHI 1500 model at TSR = 2.04

4. Multiple-Rotor Wind Turbine Aerodynamic Load Prediction using CARDAAV

The approach used to reproduce the vortex effect on aerodynamic performance of multiple-rotor wind turbine, in this case a 3-rotor configuration of the WHI 530G model, consisted of replacing in CARDAAV the uniform free stream velocity distribution by a parabolic velocity distribution as predicted by 3D CFD simulations. The parabolic velocity distribution was obtained by incorporating a free stream velocity amplification factor of 85%, i.e. $V = 1.85V_\infty$, at both extremities of the parabola and $V = V_\infty$ at its center as shown in

Figure 20. The 85% value for the velocity amplification factor was obtained from the 3D CFD runs (presented in section 7 of this report). The use of the parabolic velocity distribution predicted power coefficient values (shown in Figure 21) for the 3-rotor WHI 530G model configuration that are in excellent agreement with the field test data for the same configuration.

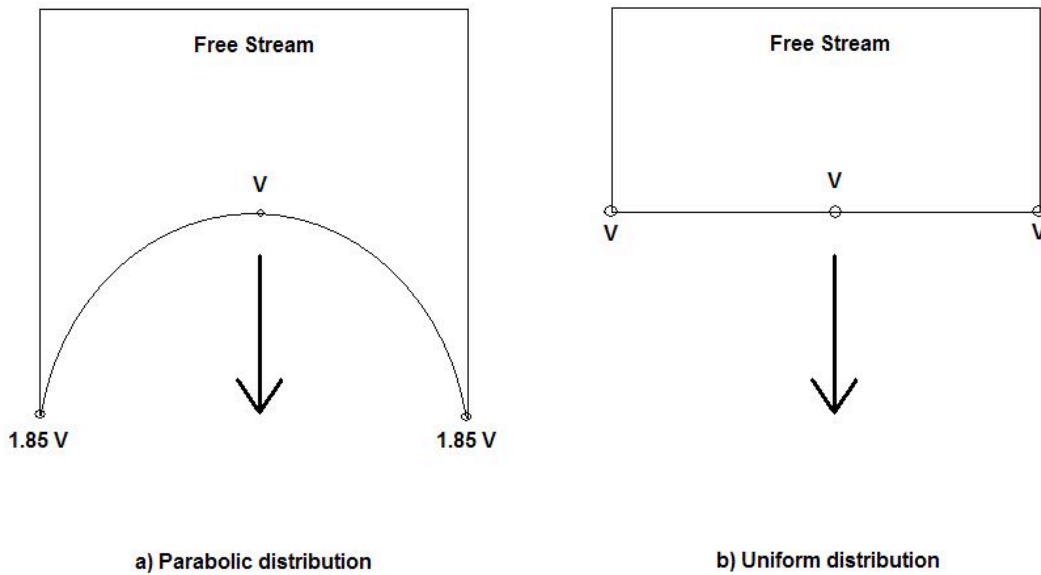


Figure 20: Free stream velocity distribution a) parabolic distribution b) uniform distribution

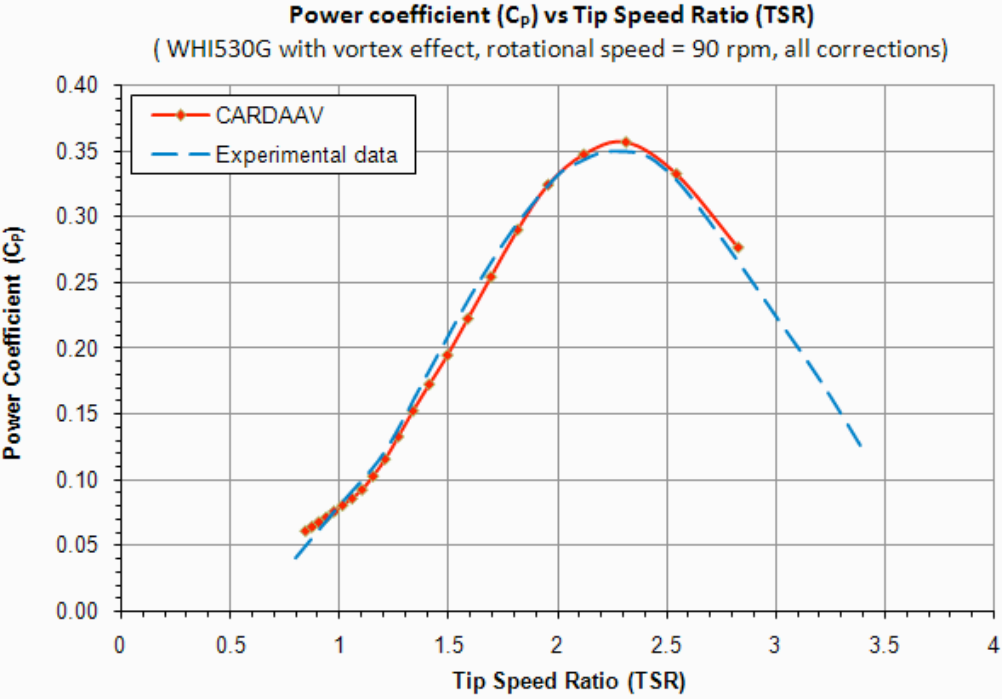


Figure 21: Performance prediction by CARDAAV using the parabolic wind distribution approach for the 3-rotor WHI 530G model

5. Isolated Rotor Wind Turbine CFD Aerodynamic Model Calibration and Validation

CFD runs were performed to simulate the flow around a 2D section (horizontal slice) of the WHI 530G model and to calculate the resulting power coefficient (C_p). The simulations are based on unsteady Reynolds Average Navier-Stokes equations coupled with the Spalard-Allmaras turbulence model. The computational domain includes two zones: a fixed zone for the far-field flow and a rotating zone that rotates with the blades. A typical four blades geometry is shown in Fig. 22. The radius of the rotating zone is $1.053 R$, where R is the radius of the rotor. Blades rotate around the central axis with angular velocity ω . For this validation case, the angular velocity is fixed at 90 rpm. The wind speed is changed to vary the tip speed ratio (TSR). Each different TSR calculation requires a different CFD run. The coefficient of power is calculated for each blade and summed up for each instantaneous time. Figure 23 shows the predicted power coefficient C_p values as a function of time for $TSR = 2$. Note that initially the C_p has a transient behavior before reaching a periodic oscillation. This behavior is typical of unsteady CFD simulations.

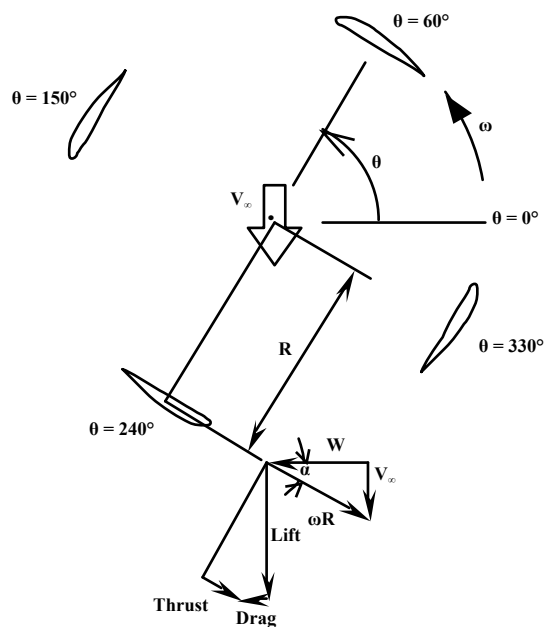


Figure 22: Typical four blade VAWT geometry.

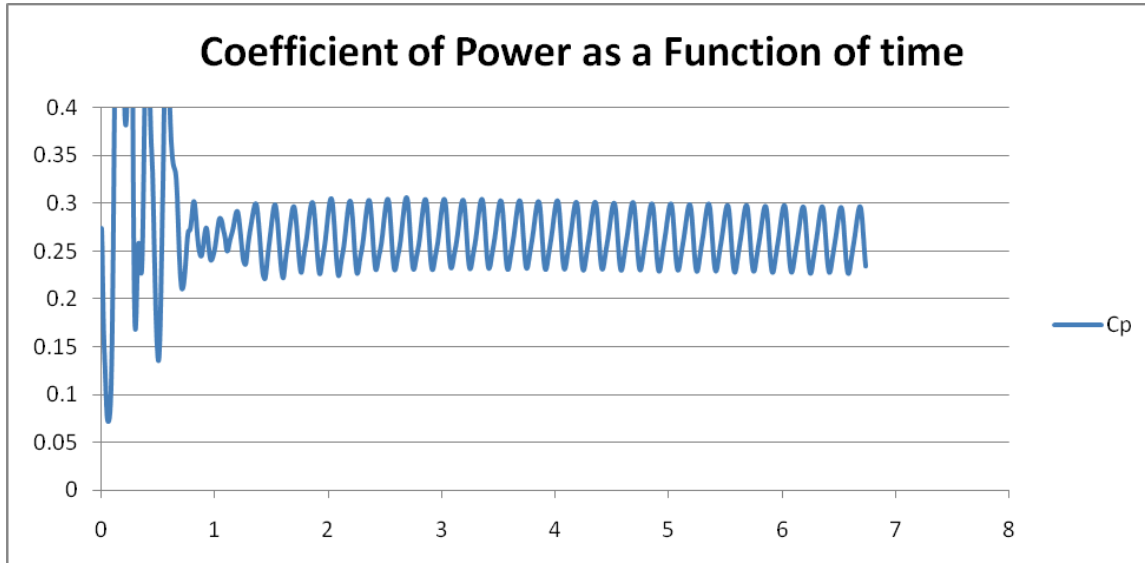


Figure 23: Predicted power coefficient C_p values as a function of time (sec) for the isolated rotor WHI 530G model at TSR = 2

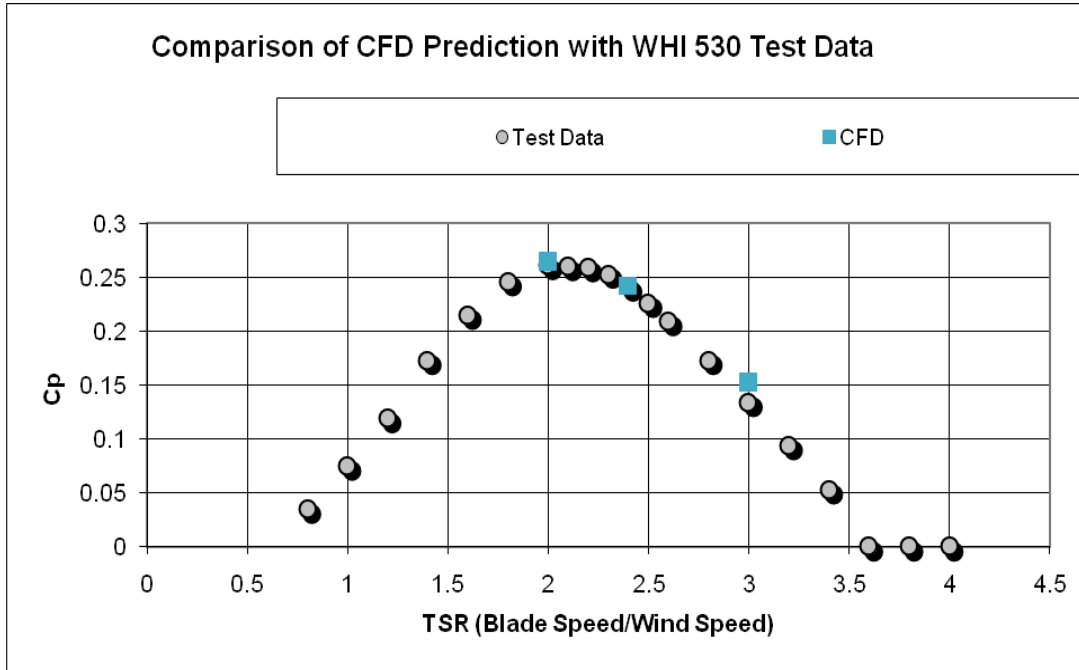


Figure 24: Comparison of CFD prediction with WHI 530G model test data.

A comparison between three different CFD runs with the WHI 530 model field test data is shown in Fig. 24 and indicates very good agreement particularly for the high power coefficient C_p values. The power coefficient C_p values of the three runs are also listed in Table 2.

Table 2: Power coefficient comparison between CFD prediction and WHI 530G model test data

Rotor configuration	CFD Prediction	Test Data Results
1 rotor TSR = 2.0	0.265	0.261
1 rotor TSR = 2.4	0.242	0.241
1 rotor TSR = 3.0	0.153	0.134
3 rotors TSR = 2.0	0.340	0.331

6. Three-Rotor Wind Turbine CFD Aerodynamic Model Load Prediction

Next, CFD runs were conducted to simulate the flow over a 3-rotor configuration of the WHI 530G model. The three rotors are arranged in a linear array along an axis perpendicular to the free stream direction. In these CFD simulations, the top rotor is rotating counter-clockwise; the middle rotor is rotating clockwise; while the bottom rotor is rotating counter-clockwise. Also, the free stream wind direction is specified as from left to right. The simulation assumes a two dimensional flow as in the case of the isolated rotor, so the flow at a constant height (in this case a horizontal slice along the rotor mid-span height) is simulated. The objective of these simulations is to study the “wake vortices” effect which is due to the proximity of two adjacent turbines placed on both sides of a turbine as shown in

Fig. 26. The distance between adjacent rotors along the array axis is 1.08 rotor diameters. The simulations were run at TSR = 2 corresponding to a wind speed of 12.65 m/s. The power coefficient (C_p) prediction for this case is 0.340. Table 2 compares the power coefficient C_p values of the CFD runs with the field test data for the isolated and 3-rotor WHI 530G model configurations.

Figures 25 and 26 show colored contour plots of the time-averaged values of the x -component of velocity U_x . The contour plots also indicate the contour level values as a legend bar on the left of the plots. Note that the average inside the circle (moving part of the domain) is not relevant as the domain rotates. A careful look at the contours in Figure 27 and 28 reveals significant acceleration of the flow between the rotors. Figure 29 shows a plot of the average x -component of velocity U_x , non-dimensionalized by the free stream velocity magnitude U_∞ , along a line in the direction of the flow that goes through the center of the middle rotor. The data is plotted only up to the beginning of the rotating zone. This flow has a sharper velocity gradient as it gets closer to the airfoil in the case of one rotor but the minimum value is the same for both cases.

Figure 30 presents the time average of the velocity in the x -direction between rotors one and two, i.e., along a line that is located at 0.54D (diameter D = 2R) from the center of the middle rotor. The dashed line represents the 3-rotor case while the solid line the single or isolated rotor case. The data for the single or isolated rotor is taken exactly at the same distance of 0.54D. Note that the flow decelerates as it approaches the blade. For the 3-rotor case, the flow acceleration just behind the blade is significantly higher than the single rotor. Figure 31 presents the average of the velocity in the x -direction between rotors two and three, similarly at 0.54D from the center of the middle rotor. Note that in this case the blades of both rotors are facing the flow and the velocity significantly increases between the blades up to a distance of 10 meters downstream of the rotors.

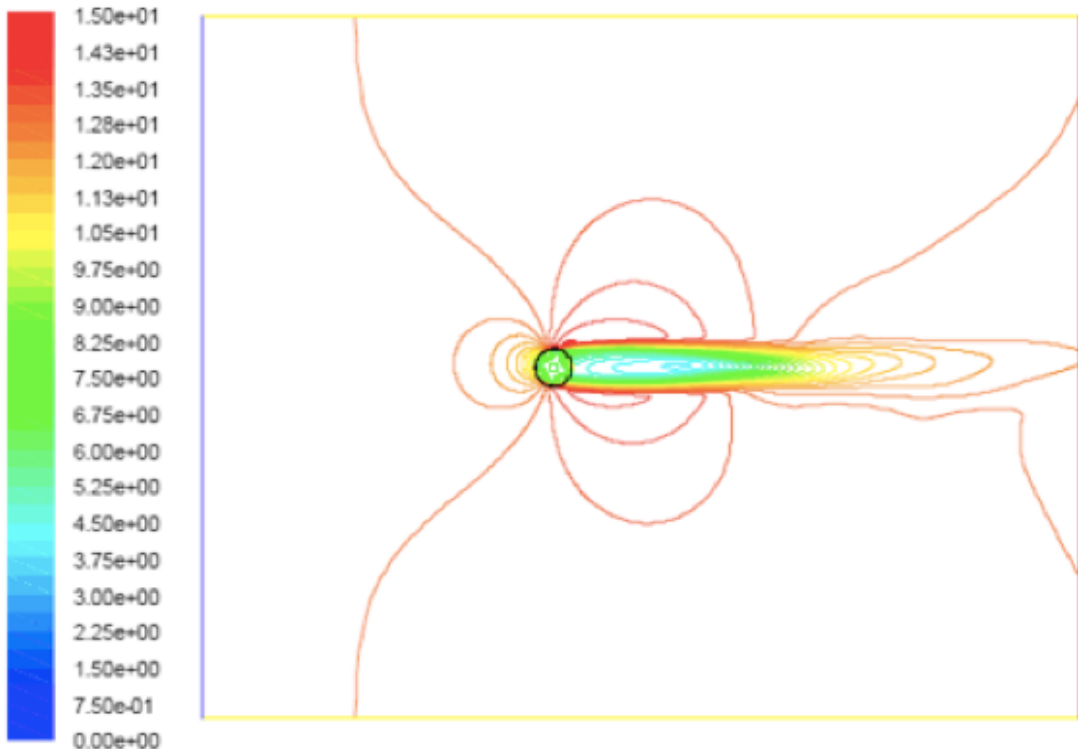


Figure 25: Contour plot of average x -velocity for single WHI 530G rotor

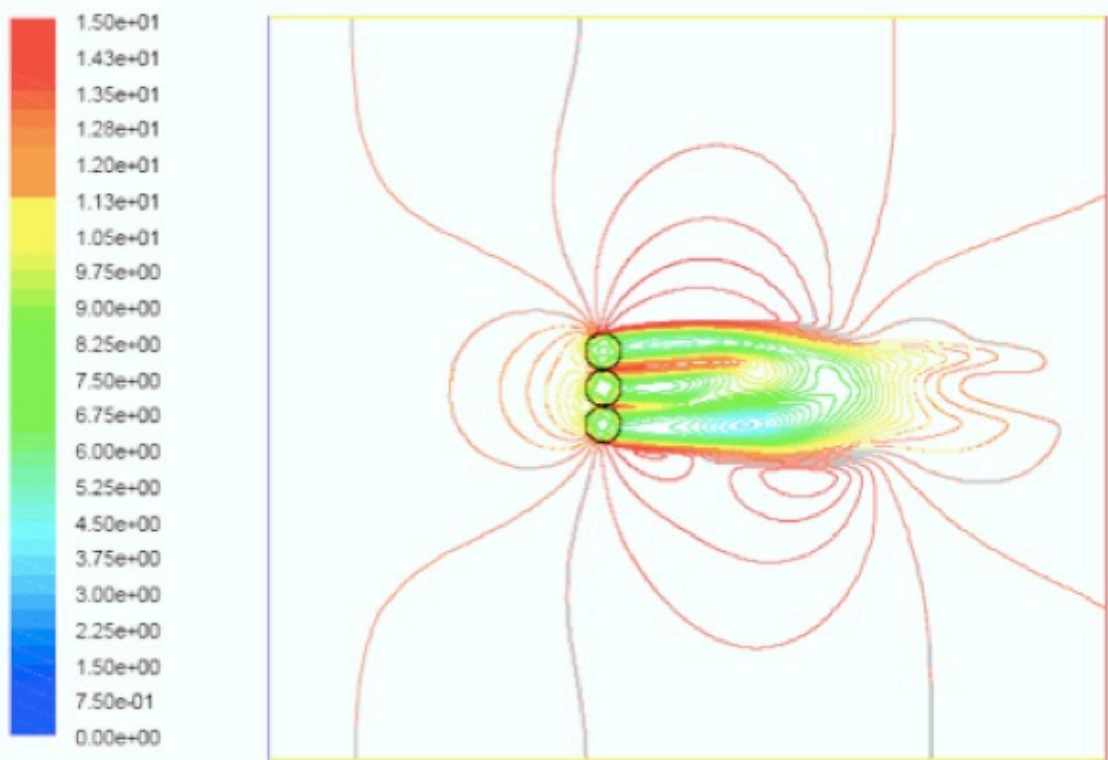


Figure 26: Contour plot of average x-velocity for the 3-rotor WHI 530G model configuration

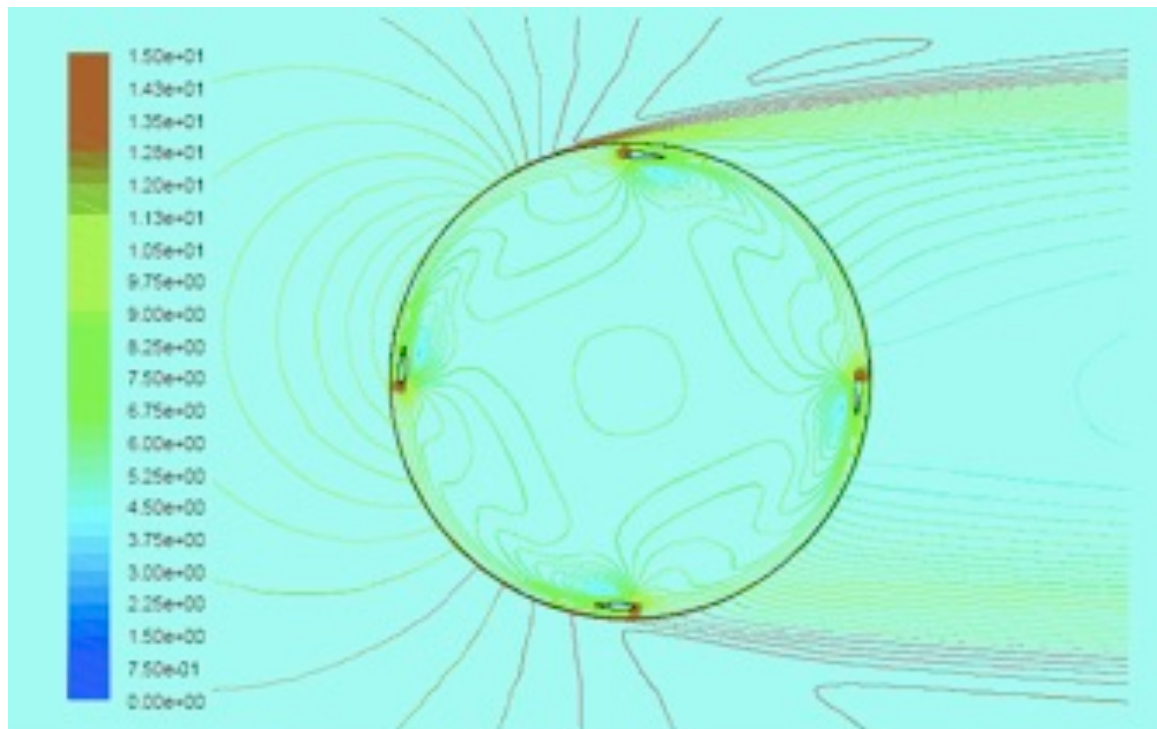


Figure 27: Close-up view of the average x-velocity contour plot for single WHI 530G rotor

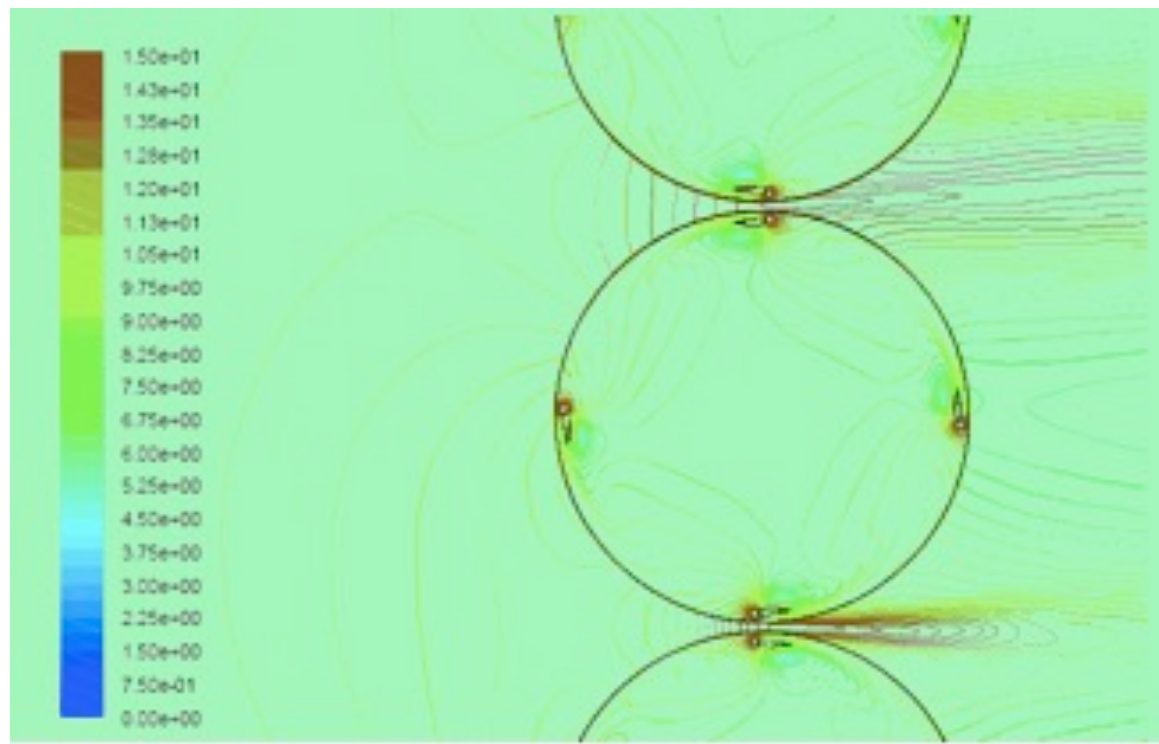


Figure 28: Close-up view of the average x-velocity contour plot for the 3-rotor WHI 530G model configuration

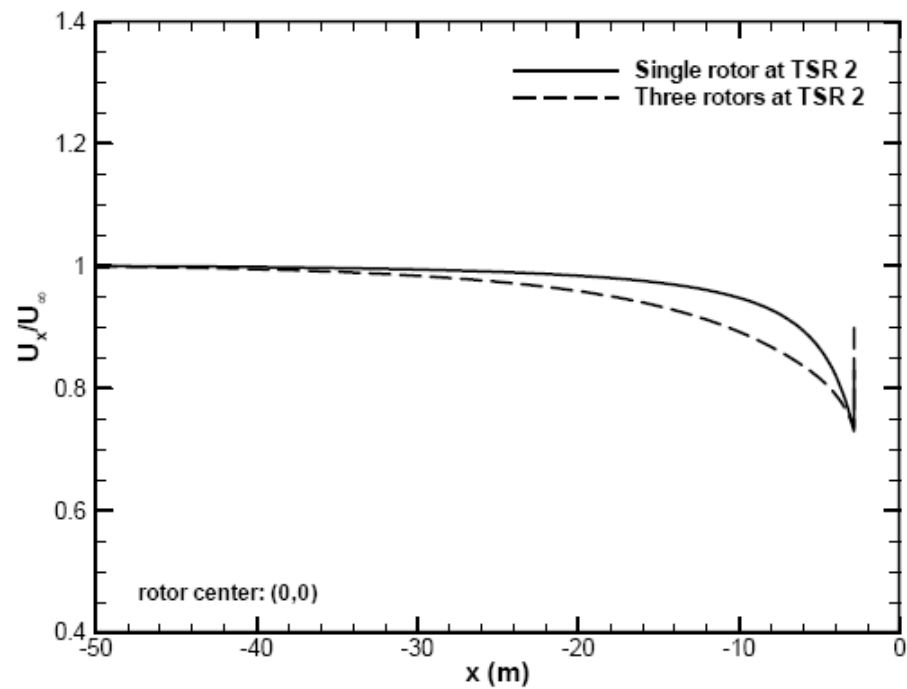


Figure 29: Comparison of x component of velocity on the center line in front of a single rotor and three rotors

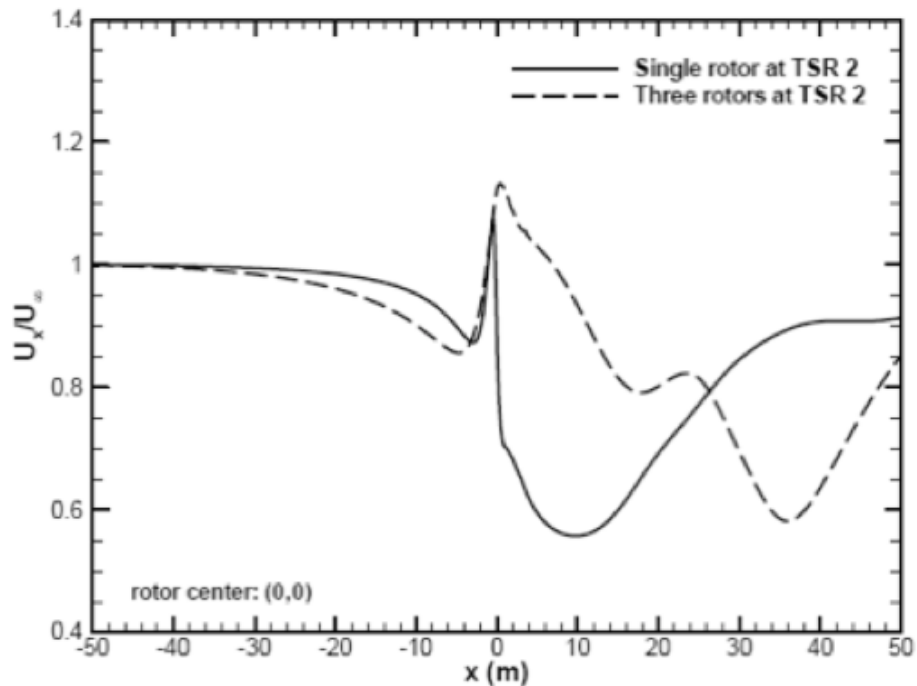


Figure 30: Comparison of x-component of velocity in between the first and the second rotors and at the same distance for one rotor.

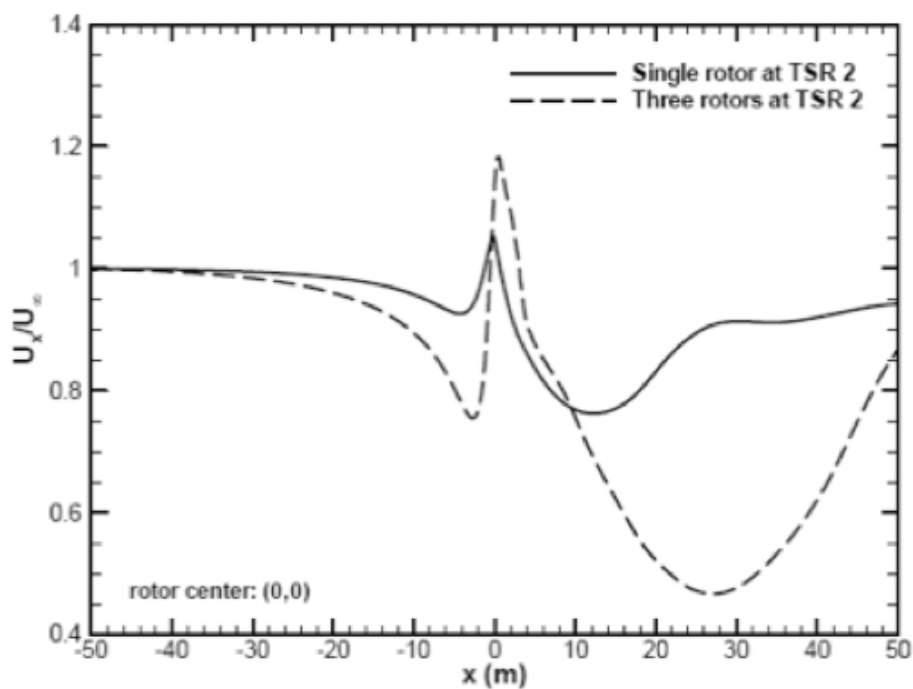


Figure 31: Comparison of x-component of velocity in between the second and the third rotor and at the same distance for one rotor.

The torque on one blade is also compared between the isolated and 3-rotor case. Figure 32 plots the torque as a function of azimuthal angle for one blade at TSR = 2. Note that the rotation of the blades is in the opposite direction because the rotor in the middle of the 3-rotor array rotates clockwise. To account for this difference the azimuthal angle is measured clockwise for the 3-rotor case. In these figures, the zero azimuthal angle corresponds to the blade located at the most upwind position. From this figure we observe that the torque is increased when the blade is in the first quadrant (-90° to 0°) and in the downwind portion of the rotor (120° to 210°). Figure 33 presents an amplification factor which is the difference of torques divided by the average torque of the single rotor case. This amplification factor reaches 2.5 in the first quadrant and 1.5 in the downwind portion of the rotor path. The surface([area?](#)) under this curve also indicates that both increases are equally important for the overall increase in torque. The average torque ratio between the three rotors case and the one rotor is 1.27 at this TSR = 2.

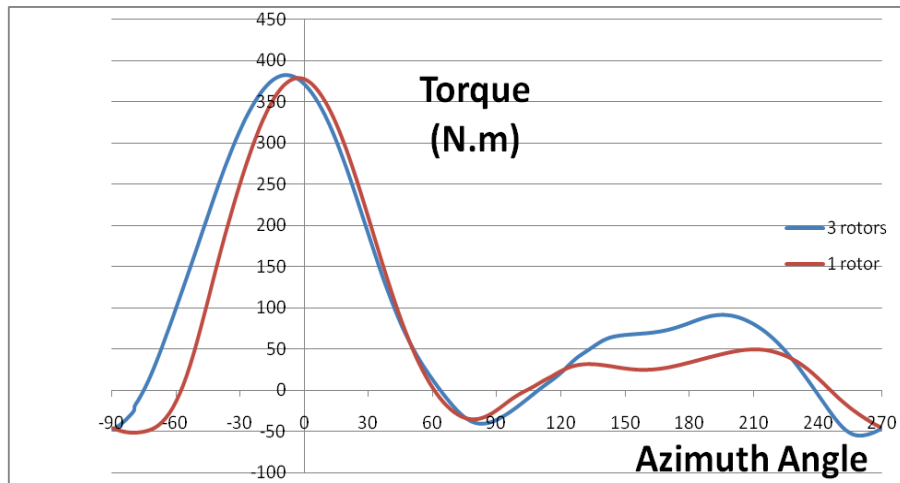


Figure 32: Comparison of torque on a single blade for the single and 3-rotor models

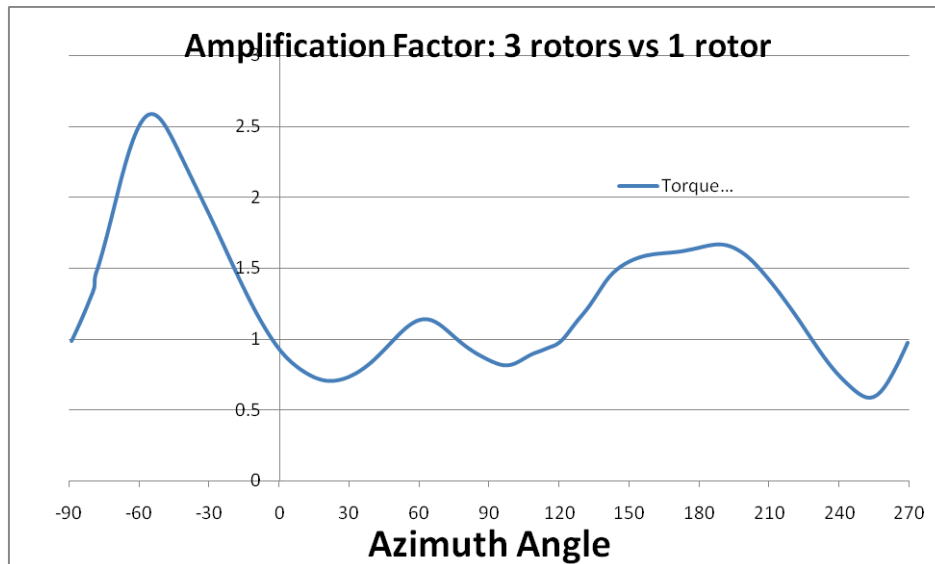


Figure 33: Amplification factor between single and 3-rotor case.

7. Parametric Study Based on 3D CFD Simulations

Parametric studies based on three-dimensional (3D) CFD simulations were performed for a 2-rotor (two side-by-side) WHI 530 rotor configuration for the case of free stream velocity $V_\infty = 11.176$ m/s, rotor rpm = 90, and rotor diameters of $D = 5.395$ m corresponding to TSR = 2.275. The rpm = 90 was chosen to compare results with available field test data for the WHI 530 model. The 3D simulations were performed to analyze the flow field around the rotors and observe any velocity augmentation or amplification effects for different rotor center-to-center distances S_c or rotor tip-to-tip distances S_t .

Figure 34 shows the flow field simulation for two side-by-side rotor configurations. In Fig. 34(a) $S_c = 15$ m and $S_t = 9.6$ m (baseline case) while in Fig. 34(b) $S_c = 7.5$ m and $S_t = 2.1$ m (halved case). The objective here was to observe any velocity or vortex augmentation effect in the region between the two rotors as the rotor center-to-center distance S_c or the rotor tip-to-tip distances S_t is decreased. The lighter shade in that region shows increased flow field velocity. The numbers 11 and 13 indicate velocity contour levels of 11 and 13 m/s, respectively.

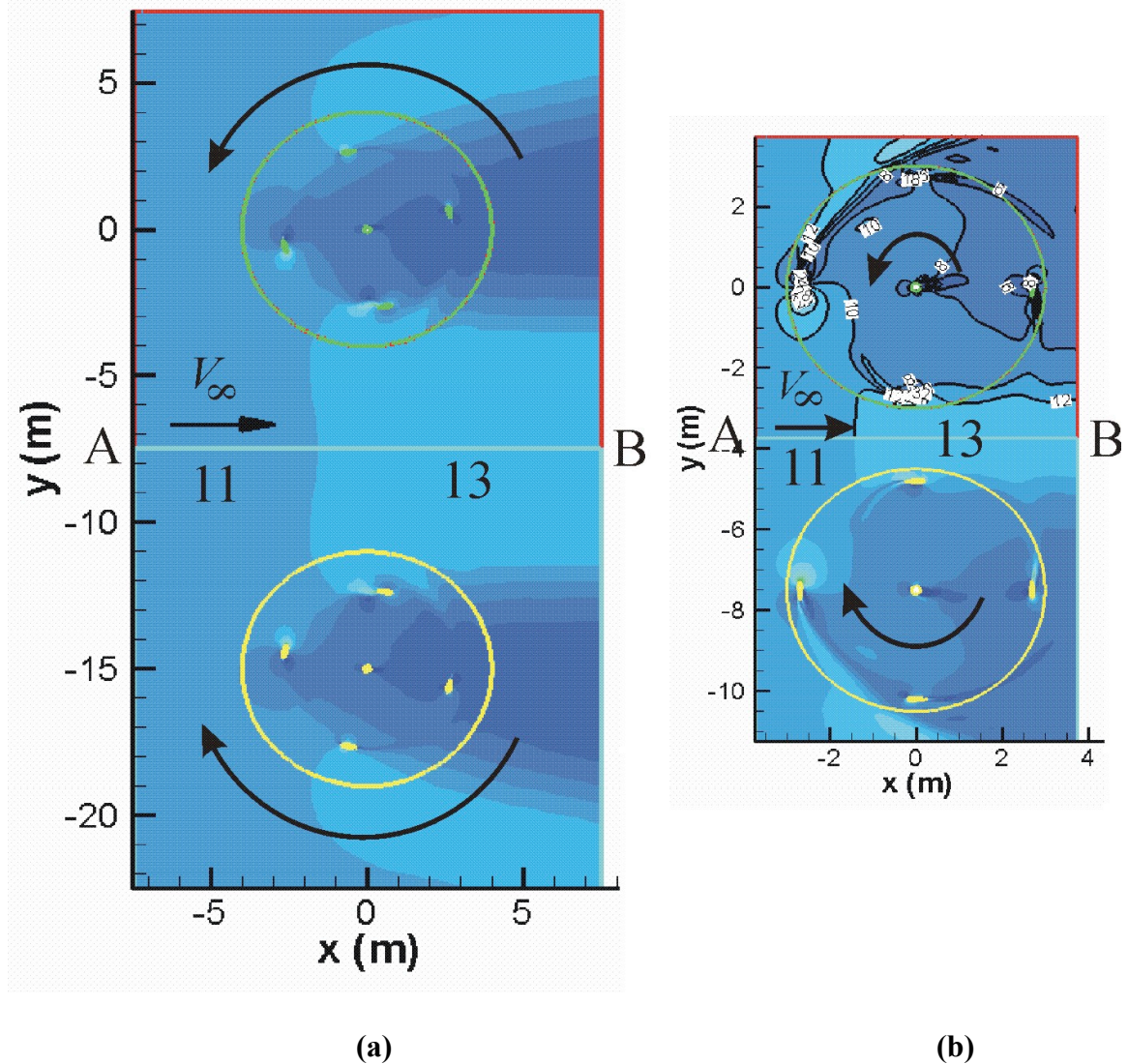


Figure 34: Side-by-side rotor flow field simulation study. (a) Baseline case $S_c = 15$ m and $S_t = 9.6$ m, (b) Halved case $S_c = 7.5$ m and $S_t = 2.1$ m.

A plot of the x -velocity component along the symmetry axis (line AB in Fig. 34) is shown in Fig. 35. The results reveal that: (1) the x -velocity component increases by 20% in the region in between the two rotors, and (2) the velocity augmentation effect is the same for two different values of the distances S_c or S_t considered.

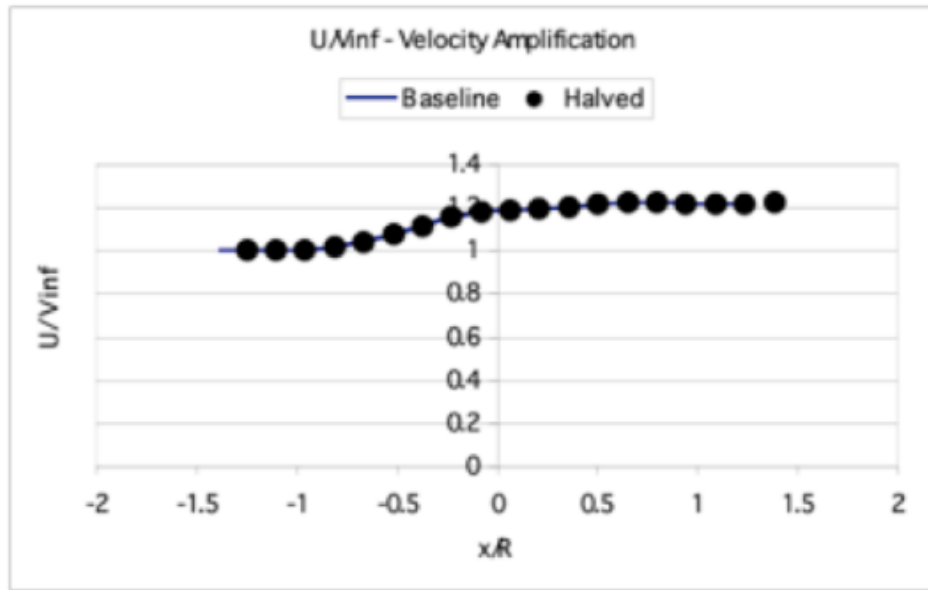


Figure 35: Plot of x -velocity component along the symmetry axis AB.

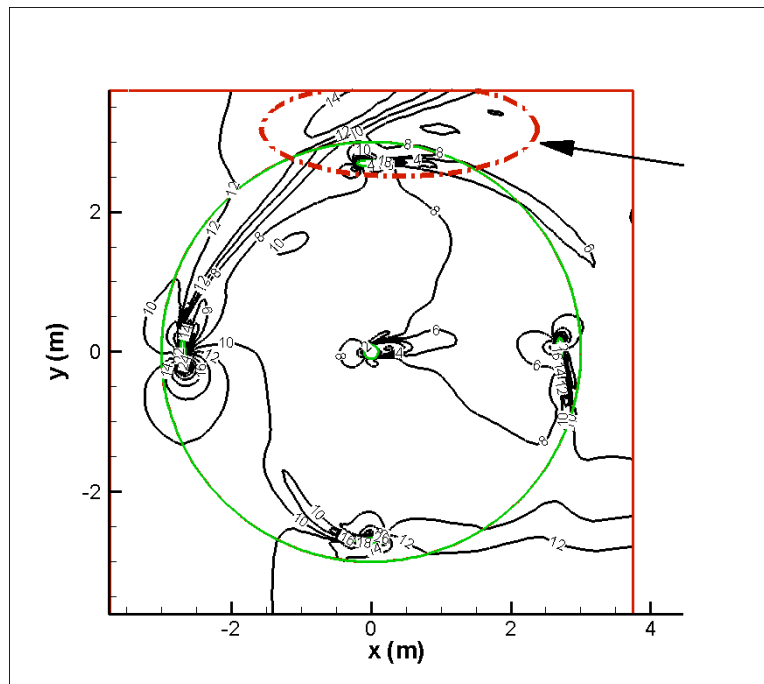


Figure 36: A close-up view of velocity contour plot for the upper rotor in Fig. 34(b) showing increased velocity levels in the region (arrow pointing at circled region) where the rotor blade is moving against the free stream direction.

The simulation results also reveal an important flow field feature that the velocity augmentation effect is higher in regions where the rotor blade is moving against the free stream flow direction (see circled region in Fig. 36 above). This observation suggests that to further boost the augmentation affect, the rotor rotations must be reversed in Fig. 34 so that the rotor blades of two side-by-side rotors are moving against the free stream direction along the symmetry axis (line AB). Therefore, the halved case [Fig. 34(b)] was run with the rotor rotation directions reversed. This is referred to as the halved-reversed case. A comparison of the x -velocity component along the symmetry axis (line AB) for all of the three cases investigated is shown in Fig. 37. The results indicate that for the halved-reversed case, the x -velocity component increases to 53% in the region between the two rotors. The results therefore confirm that to get maximum velocity augmentation, the preferred rotor configuration is the one with blades moving opposite the free stream direction in the region between the two rotors.

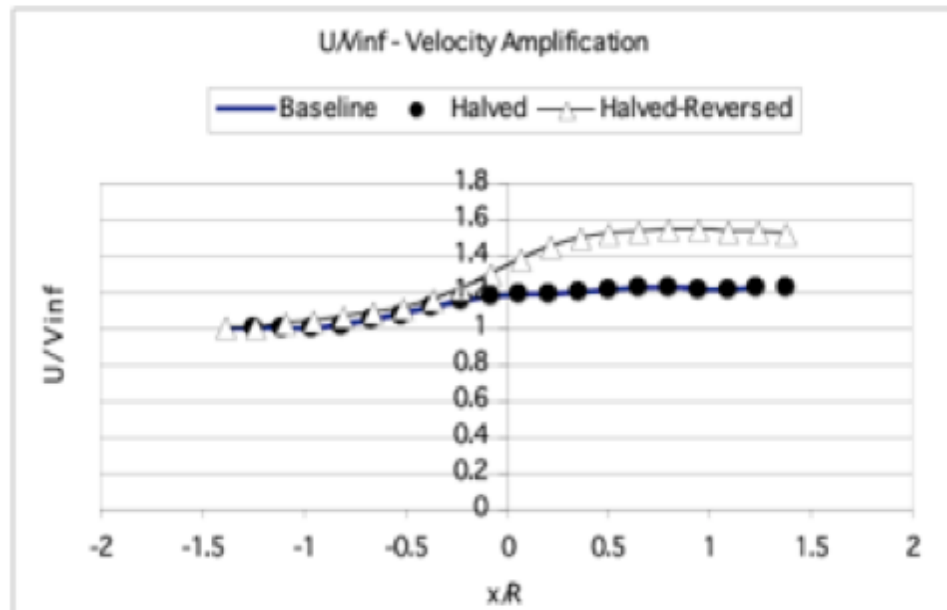


Figure 37: A comparison of x -velocity component along the symmetry axis (AB) for the three cases investigated.

Figure 38 shows the detailed flow field velocity contour levels for the halved-reversed case study. It can be seen that the velocity magnitude increase from a free stream value of about 11.176 m/s to more than 17 m/s along the axis of symmetry.

Figures 39 and 40 show the velocity contour plots for two 3D CFD simulation runs for tip-to-tip distances S_t of 1.105 and 1.0525 m, respectively. Note that the $S_t = 1.0525$ m corresponds to the actual 3-rotor field test WHI 530G model. The simulations predict velocity amplification by almost 76% and 85% for tip-to-tip distances S_t of 1.105 and 1.0525 m, respectively.

A comparison of the non-dimensional x -velocity amplification plot along the axis of symmetry versus the rotor tip-to-tip clearance distance for the different cases investigated in this study is shown in Fig. 41.

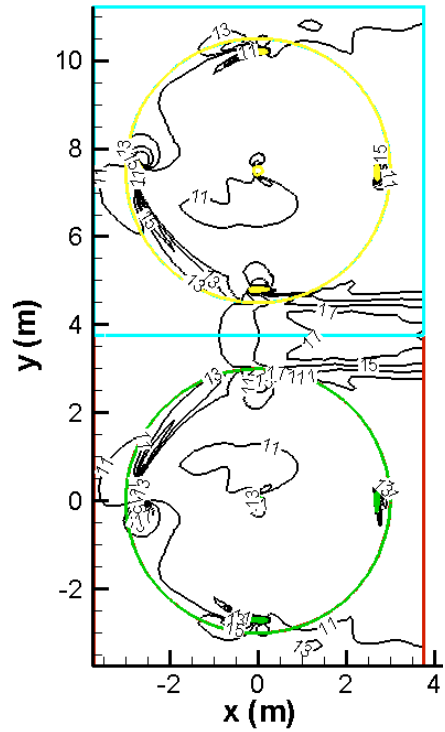


Figure 38: Side-by-side rotor flow field simulation study showing velocity contours for the halved-reversed case study ($S_c = 7.5$ m and $S_t = 2.1$ m).

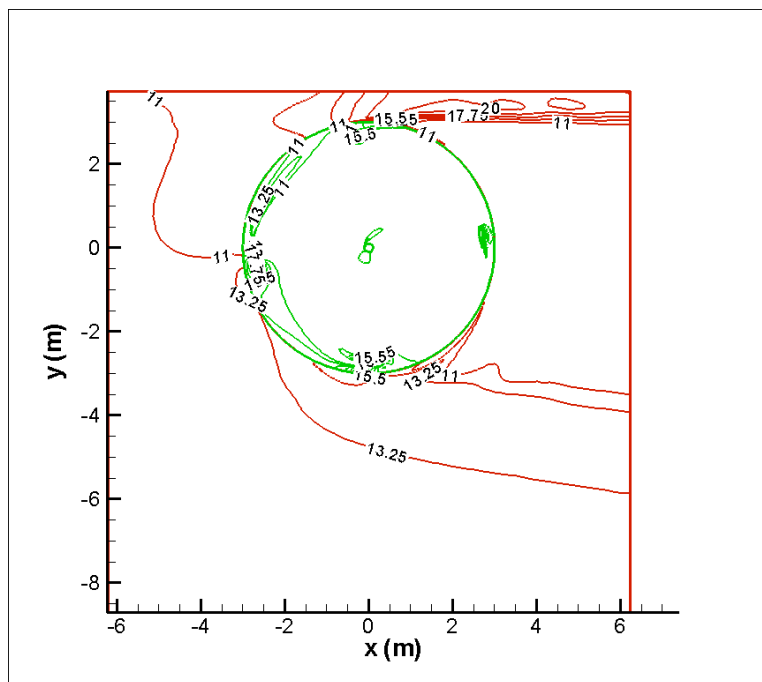


Figure 39: Side-by-side rotor flow field simulation showing velocity contours for the $S_t = 1.105$ m case.

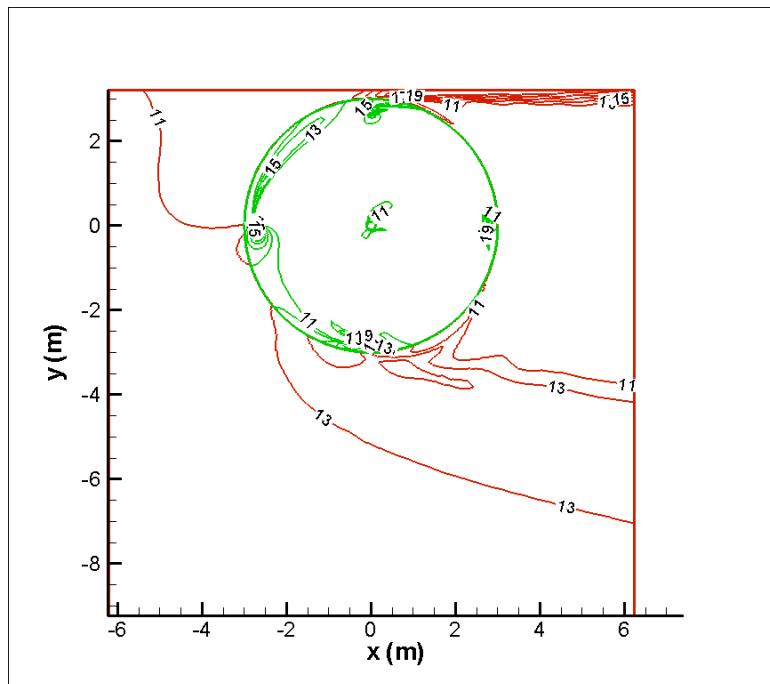


Figure 40: Side-by-side rotor flow field simulation showing velocity contours for the $S_t = 1.0525$ m case (similar to the 3-rotor WHI 530G field test model).

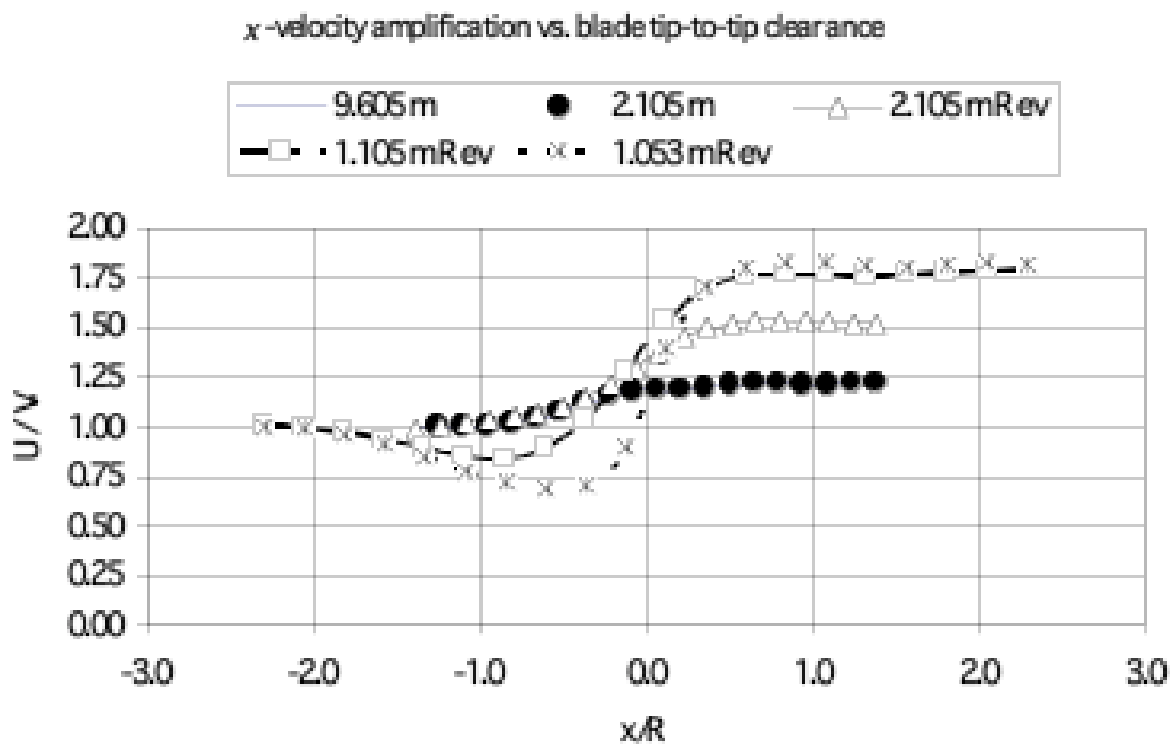


Figure 41: A comparison of x-velocity component along the symmetry axis (AB) for the different 3D CFD simulation cases investigated.

The 3D simulations results confirm 2D simulations results for tip clearance distance close to 1 m. There is a dip in the x-velocity component upstream of the 90-deg location (top location during rotation) which rises sharply as the blades cross the 90-deg location to almost 185% of the free stream value. Thus the blade sees a flow that is accelerating in the region. This may give a significant boost to the local power coefficient values. To determine the effect of this velocity amplification on the power coefficient, a parabolic velocity amplification distribution was used in CARDAAV. The results of this analysis are presented in section 4 of this report. The results show that the use of the parabolic velocity distribution predicted power coefficient values (shown in Figure 21) for the 3-rotor WHI 530G model configuration that are in excellent agreement with the field test data for the same configuration. {Why can't a Cp amplification factor be calculated as a function of St if velocity amplification can be calculated as a function of St and since it has been found that 2D simulations give accurate results? {Yes, a Cp amplification factor is also possible and this fact was proposed by Prof. Marius. Since the velocity amplification varies along the azimuthal position, at first, we thought of looking at the velocity variations and use that to compute the Cp - FS}}

Can't these analyses (velocity and Cp magnification) be made on the Model 1500? If not why not? RNT. {yes, the CFD studies can provide insight into this fact and more on the scale and other effects through parametric studies as suggested in the proposal. However, this requires very extensive computational effort and resources. - FS}

8. Conclusions

In this work it is shown that both CARDAAV code and CFD simulations can predict accurate estimates of the power coefficient with and without the vortex effect. The effect of vortex augmentation is predicted with a good degree of accuracy using CFD compared to the field test data. Nevertheless CFD simulations require significant calibration because the turbulence model is not well adapted for highly separated boundary layer flow. Note also that the CFD is very sensitive to the mesh characteristics. The CFD runs require long computational time. Each TSR run takes about three days on an eight processor computer. Use of parabolic free stream velocity distribution in CARDAAV with amplification factors derived from the CFD simulations was found to predict power coefficient in good agreement with field test data.

The comparison between single rotor and 3-rotor models clearly demonstrates that the proximity of the rotors increases the power coefficient. The analysis also shows that the increase in the torque magnitude or velocity amplification is greater on the advancing blades, i.e., blades moving against the free stream direction as well as when the tip-to-tip distance is decreased.

9. Future Work

Although, the study has helped validate the vortex augmentation effect based on a fixed geometry and orientation with respect to the wind direction, much still remains to be investigated to accurately ascertain the overall impact of multiple rotor configurations. For example, the multiple rotor case investigated in this report is strictly dependent on the orientation of the rotor with respect to the wind direction. Questions, such as how a change in wind direction or blade shape or rotor solidity or a combination of such variables will affect the vortex augmentation effect, still remain to be addressed. The CFD analysis can be used to address these concerns and identify the best placement of the rotors. Parameters such as distance between rotors and linear array versus a staggered configuration can also

be analyzed. The effects of the wind vector for the linear array of rotors can also be simulated to determine how it affects power output. Thus, it becomes imperative that follow-on CFD simulations be carried out to address these concerns and determine the true nature and scope of the vortex augmentation effect as well as establish its analysis capability. As an example, the following tasks can be accomplished by the developed CFD methodology:

- Calculation of the coefficient of power for different rotor sizes of the same type;
- Investigation of distance between rotors;
- Placement and rotor array configuration;
- Wind variation both temporal and direction.

10. Appendix 1

Table 1 : Power coefficient (C_p) vs tip speed ratio (TSR) for the WHI530G at 90 rpm

TSR	C_p	
	No vortex effect	With vortex effect
0.8767	0.0573	0.0635
0.9416	0.0674	0.0707
1.0169	0.0794	0.0800
1.1054	0.0996	0.0918
1.2106	0.1297	0.1150
1.3381	0.1633	0.1517
1.4955	0.1985	0.1941
1.6949	0.2331	0.2537
1.9556	0.2596	0.3237
2.3112	0.2502	0.3562
2.8248	0.1709	0.2760

Table 2 : Power coefficient (C_p) vs tip speed ratio (TSR) for the WHI1500 (6 blades) at 41 rpm

TSR	C_p
0.8809	0.0461
0.9462	0.0543
1.0219	0.0652
1.1107	0.0796
1.2165	0.1008
1.3445	0.1383
1.5027	0.1919
1.7031	0.2394
1.9651	0.2943
2.3224	0.3129
2.8385	0.2960

Table 3 : Normal and tangential force (N) for 1 blade and rotor torque (N.m) vs azimuthal angle (deg.) for the WHI530G at 90 rpm, TSR = 1.02

Azimuthal angle (deg.)	Normal (N)	Tangential (N)	Torque (Nm)
-89.69	-91.2568	-46.8185	668.7525
-59.69	-7413.0892	1745.7819	3849.9470
-29.69	-6391.8778	2523.2910	6229.5625
0.31	-3680.1177	1056.1132	668.7525
30.31	-2125.3285	619.2254	3849.9470
60.31	-607.5434	170.0708	6229.5625
90.31	0.4879	-6.1490	668.7525
120.31	607.8741	67.3931	3849.9470
150.31	2593.0532	-303.9604	6229.56245
180.31	5069.1177	-738.0450	668.7525
210.31	5163.7604	-911.3171	3849.9470
240.31	3374.5527	-116.1779	6229.5625

Table 4 : Normal and tangential force (N) along the length (m) of a single blade for the WHI530G at 90 rpm, TSR = 1.02

HZ (m)	-47.2 deg.		194.7 deg.	
	Normal (N)	Tangential (N)	Normal (N)	Tangential (N)
-4.35	-229.82	41.00	99.89	-10.48
-3.92	-347.85	94.73	123.82	-27.12
-3.48	-379.72	115.70	144.45	-30.28
-3.05	-400.31	128.37	154.77	-31.94
-2.61	-412.45	135.93	161.17	-33.10
-2.18	-421.68	141.28	166.14	-33.88
-1.74	-428.82	145.30	170.32	-34.53
-1.31	-434.80	148.62	174.06	-35.10
-0.87	-440.35	151.63	177.52	-35.60
-0.44	-445.57	154.42	180.78	-36.07
0.00	-450.53	157.05	183.88	-36.49
0.44	-455.19	159.47	186.81	-36.89
0.87	-459.59	161.72	189.58	-37.25
1.31	-463.64	163.71	192.14	-37.59
1.74	-466.93	165.14	194.35	-37.89
2.18	-469.46	165.76	195.87	-38.14
2.61	-470.11	164.58	195.94	-38.30
3.05	-466.69	159.65	192.82	-38.24
3.48	-454.06	146.99	182.75	-37.52
3.92	-413.82	118.24	158.31	-34.05
4.35	-283.25	52.13	117.73	-14.18

Table 5 : Normal and tangential force (N) for 1 blade and rotor torque (N.m) vs azimuthal angle (deg.) for the WHI530G at 90 rpm, TSR = 2.03

Azimuthal angle (deg.)	Normal (N)	Tangential (N)	Torque (Nm)
-89.69	-34.3182	-26.8396	1857.3753
-59.69	-2679.0399	374.7689	1771.2910
-29.69	-3470.0611	868.5856	1992.2770
0.31	-2675.1017	873.3292	1857.3753
30.31	-1105.0891	-98.4484	1771.2910
60.31	-492.6498	-176.3226	1992.2770
90.31	4.0043	-139.2512	1857.3753
120.31	1174.9875	303.6553	1771.2910
150.31	1256.7545	182.2929	1992.2770
180.31	21.1057	-11.8990	1857.3753
210.31	20.3031	-12.3445	1771.2910
240.31	991.9467	51.3010	1992.2770

Table 6 : Normal and tangential force (N) along the length (m) of a single blade for the WHI530G at 90 rpm, TSR = 2.03

HZ (m)	-30.3 deg.		134.7 deg.	
	Normal (N)	Tangential (N)	Normal (N)	Tangential (N)
-4.35	-131.2099	25.7902	61.2781	12.0603
-3.92	-146.8059	32.6156	73.3941	17.0189
-3.48	-151.2359	34.4305	75.8454	18.4238
-3.05	-155.1387	36.0397	77.2602	19.3123
-2.61	-158.7565	37.5516	78.4115	20.0811
-2.18	-162.1361	38.9846	79.3857	20.7562
-1.74	-165.3043	40.3175	80.2704	21.3838
-1.31	-168.2894	41.5699	81.0827	21.976
-0.87	-171.1175	42.7692	81.8215	22.5847
-0.44	-174.0025	44.0054	82.4009	23.142
0.00	-176.5633	45.1133	82.7244	23.6105
0.44	-179.0138	46.1807	82.7272	23.9688
0.87	-181.3202	47.1976	82.7508	24.3208
1.31	-183.4623	48.1625	82.7906	24.665
1.74	-185.5311	49.1008	82.8429	25.0024
2.18	-186.9562	49.8555	81.2033	22.0674
2.61	-188.3381	50.5904	81.6654	22.4544
3.05	-189.6738	51.3020	82.0761	22.8145
3.48	-190.9053	51.9359	82.1754	23.0417
3.92	-191.0138	51.6536	80.8475	22.5968

Table 7 : Normal and tangential force (N) for 1 blade and rotor torque (N.m) vs azimuthal angle (deg.) for the WHI1500 at 41 rpm, TSR = 1.00

Azimuthal angle (deg.)	Normal (N)	Tangential (N)	Torque (Nm)
-89.69	-172.7947	-86.1459	14948.2682
-59.69	-13793.8793	3237.3705	24963.2654
-29.69	-10915.7744	2962.0462	14948.2682
0.31	-7054.1712	841.0292	24963.2654
30.31	-4088.7746	342.1827	14948.2682
60.31	-1171.7452	19.6490	24963.2654
90.31	0.6125	-14.8380	14948.2682
120.31	1149.4185	15.3999	24963.2654
150.31	3805.1260	-165.6978	14948.2682
180.31	5930.0809	-629.1921	24963.2654
210.31	6511.0353	-510.9023	14948.2682
240.31	7567.5141	720.5270	24963.2654

Table 8 : Normal and tangential force (N) along the length (m) of a single blade for the WHI1500 at 41 rpm, TSR = 1.00

HZ (m)	-50.9 deg.		217.8 deg.	
	Normal (N)	Tangential (N)	Normal (N)	Tangential (N)
-5.67	-380.0177	57.8062	248.4936	39.4910
-5.10	-570.1465	135.4421	273.1972	-0.8010
-4.53	-626.4983	169.4270	295.0818	-7.1872
-3.97	-664.1499	186.8743	311.1488	-7.5126
-3.40	-688.2558	196.2308	322.8205	-7.5507
-2.83	-706.7935	203.0470	331.7990	-7.8779
-2.27	-721.4162	208.2547	336.1898	-10.0194
-1.70	-735.3055	213.0480	340.3944	-11.8855
-1.13	-747.3195	217.1328	344.3442	-13.5573
-0.57	-758.3341	221.8295	348.0996	-15.1073
0.00	-768.7266	226.2370	351.9955	-16.6504
0.57	-778.0428	230.1111	355.6510	-17.9394
1.13	-785.6818	233.2968	359.1580	-19.1294
1.70	-792.7344	236.0529	362.5409	-20.1764
2.27	-798.8565	238.0794	365.8008	-20.9652
2.83	-803.4460	238.7858	368.9349	-21.2457
3.40	-805.5904	237.0672	371.9388	-20.4762
3.97	-797.7388	230.8850	374.8269	-17.4711
4.53	-772.3283	218.7078	378.9351	-9.3773
5.10	-700.9855	175.8396	356.3977	-5.8901
5.67	-483.0016	75.8601	316.2479	53.7010

Table 9 : Normal and tangential force (N) for 1 blade and rotor torque (N.m) vs azimuthal angle (deg.) for the WHI1500 at 41 rpm, TSR = 2.04

Azimuthal angle (deg.)	Normal (N)	Tangential (N)	Torque (Nm)
-89.69	-63.9616	-48.8531	10316.6625
-59.69	-4995.0905	696.76565	15011.0906
-29.69	-6266.0167	1565.7075	10316.6625
0.31	-4591.8320	1299.6900	15011.0906
30.31	-2122.4506	-105.2920	10316.6625
60.31	-980.4683	-189.6429	15011.0906
90.31	5.1944	-138.3775	10316.6625
120.31	2043.4819	433.2659	15011.0906
150.31	2915.9501	572.8335	10316.6625
180.31	1201.7552	79.8491	15011.0906
210.31	749.3701	18.1638	10316.6625
240.31	2067.5904	136.3872	15011.0906

Table 10 : Normal and tangential force (N) along the length (m) of a single blade for the WHI1500 at 41 rpm, TSR = 2.04

HZ (m)	-31.6 deg.		149.7 deg.	
	Normal (N)	Tangential (N)	Normal (N)	Tangential (N)
-5.67	-232.7567	42.6043	116.1280	17.0691
-5.10	-266.3035	56.7169	124.2231	19.2605
-4.53	-275.8436	60.5792	129.4867	21.2044
-3.97	-283.4283	63.7748	135.2503	23.5011
-3.40	-288.539	66.3223	140.3591	25.6820
-2.83	-293.3336	68.7305	144.8450	27.6870
-2.27	-297.850	71.0159	146.5769	29.1675
-1.70	-302.0598	73.0970	137.4604	24.4261
-1.13	-305.9836	74.9879	140.9733	25.9506
-0.57	-310.1679	76.9109	144.0410	27.3198
0.00	-314.3957	78.8151	145.7232	28.4201
0.57	-318.4206	80.6413	146.7861	29.3495
1.13	-322.2658	82.3982	147.7863	30.2507
1.70	-325.9459	84.0912	148.7052	31.1192
2.27	-329.4771	85.7260	149.9223	32.0357
2.83	-332.8729	87.3059	151.2701	32.9719
3.40	-336.1398	88.8317	152.6035	33.9179
3.97	-339.1876	90.2588	153.9253	34.8743
4.53	-341.4345	91.2571	155.2508	35.9487
5.10	-339.1734	89.2971	155.4181	36.7701
5.67	-291.7262	60.6679	137.8349	29.4865